ISSN 2667-4211

ESKİŞEHİR TECHNICAL UNIVERSITY JOURNAL OF SCIENCE AND TECHNOLOGY

A – Applied Sciences and Engineering

Volume 23 Number 3 - September - 2022

ESKİŞEHİR TECHNICAL UNIVERSITY JOURNAL OF SCIENCE AND TECHNOLOGY
A- Applied Sciences and Engineering
Eskişehir Teknik Üniversitesi Bilim ve Teknoloji Dergisi A – Uygulamalı Bilimler ve Mühendislik

Volume: 23 / Number: 3 / September - 2022

Eskişehir Technical University Journal of Science and Technology A - Applied Sciences and Engineering (ESTUJST-A) is a peer-reviewed and refereed international journal published by Eskişehir Technical University. Since 2000, it has been regularly published and distributed biannually and it has been published quarterly and only electronically since 2016.
The journal accepts only manuscripts written in English.

The journal issues are published electronically in **March, June**, **September**, and **December**.

Eskişehir Technical University Journal of Science and Technology A - Applied Sciences and Engineering is an international peer-reviewed and refereed journal published by Eskişehir Technical University.

The journal is dedicated to the dissemination of knowledge in applied sciences and engineering disciplines.

The journal aims to publish high quality, original international scientific research articles with specific contributions to the literature in the field of engineering and applied sciences. The journal publishes research papers in the fields of applied science and technology such as Physics, Biology, Mathematics, Statistics, Chemistry and Chemical Engineering, Environmental Sciences and Engineering, Civil Engineering, Earth and Atmospheric Sciences, Electrical and Electronical Engineering, Computer Science and Informatics, Materials Sciences and Engineering, Mechanical Engineering, Mining Engineering, Industrial Engineering, Aeronautics and Astronautics, Pharmaceutical Sciences.

The journal publishes original research articles and special issue articles. All articles are peer-reviewed and the articles that have been evaluated are ensured to meet with researchers as soon as possible.

Eskişehir Technical University holds the copyright of all published material that appear in Eskişehir Technical University Journal of Science and Technology A - Applied Sciences and Engineering.

"Anadolu Üniversitesi Bilim ve Teknoloji Dergisi A - Uygulamalı Bilimler ve Mühendislik (Anadolu University Journal of Science and Technology A - Applied Sciences and Engineering)" published within Anadolu University started to be published within Eskişehir Technical University which was established due to statute law 7141, in 2018. Hence, the name of the journal is changed to " Eskişehir Technical University Journal of Science and Technology A - Applied Sciences and Engineering (Eskişehir Teknik Üniversitesi Bilim ve Teknoloji Dergisi A - Uygulamalı Bilimler ve Mühendislik)".

Indexed by **DOAJ** - Directory of Open Access Journals, **EBSCO** and **ULAKBIM**

ESKİŞEHİR TECHNICAL UNIVERSITY JOURNAL OF SCIENCE AND TECHNOLOGY
A- Applied Sciences and Engineering
Eskişehir Teknik Üniversitesi Bilim ve Teknoloji Dergisi A – Uygulamalı Bilimler ve Mühendislik

Volume: 23 / Number: 3 / September – 2022

Owner / Publisher: Prof. Dr. Adnan ÖZCAN for Eskişehir Technical University

EDITOR-IN-CHIEF
Prof. Dr. Murat TANIŞLI
Eskişehir Technical University, Institute of Graduate Programs, 26470 Eskişehir, TURKEY
Phone: +90 222 213 7470
e-mail: mtanisli@eskisehir.edu.tr

CO-EDITOR IN CHIEF
Assoc. Prof. Dr. Tuğba ARAS
Eskişehir Technical University, Institute of Graduate Programs, 26470 Eskişehir, TURKEY
Phone: +90 222-213 7472
e-mail: tugbasoganci@eskisehir.edu.tr

CO-EDITOR IN CHIEF
Assit. Prof. Dr. Hüseyin Ersin EROL
Eskişehir Technical University, Institute of Graduate Programs, 26470 Eskişehir, TURKEY
Phone: +90 222-213 7473
e-mail: tugbasoganci@eskisehir.edu.tr

CONTACT INFORMATION
Eskişehir Technical Unıversity Journal of Science and Technology
Eskişehir Technical University, Institute of Graduate Programs, 26470 Eskişehir, TURKEY
Phone: +90 222 213 7485
e-mail : btda@eskisehir.edu.tr

ESKİŞEHİR TECHNICAL UNIVERSITY JOURNAL OF SCIENCE AND TECHNOLOGY
A- Applied Sciences and Engineering

Eskişehir Teknik Üniversitesi Bilim ve Teknoloji Dergisi A – Uygulamalı Bilimler ve Mühendislik

Volume: 23 / Number: 3 / September - 2022

OWNER

Adnan ÖZCAN, **The Rector of Eskişehir Technical University**

EDITORIAL BOARD

Murat TANIŞLI, **Editor in Chief**

Tuğba ARAS, **Co-Editor in Chief**

Hüseyin Ersin EROL, **Co-Editor in Chief**

LANGUAGE EDITOR-ENGLISH

İlker DEMİROĞLU

SECTION EDITORS

Emin AÇIKKALP (ESTU, Turkey)
Şener AĞALAR (ESTU, Turkey)
Ziya AKÇA (Eskisehir Osmangazi University, Turkey)
Haydar ARAS (Eskisehir Osmangazi University, Turkey)
Tuğba ARAS (ESTU)
Funda ATEŞ (ESTU, Turkey)
Uğur AVDAN (ESTU, Turkey)
Nezihe AYAS (ESTU, Turkey)
Doç. Dr. Rukiye AYRANCI (Kütahya Dumlupınar University)
Özge BAĞLAYAN (ESTU, Turkey)
Recep BAKIŞ (ESTU, Turkey)
Müfide BANAR (ESTU, Turkey)
Ayşe H. BİLGE (Kadir Has University, Turkey)
Mehmet CANDAN (ESTU, Turkey)
Özgür CEYLAN (ESTU, Turkey)
Rasime DEMİREL (ESTU, Turkey)
İlker DEMİROĞLU (ESTU, Turkey)
Sedef DİKMEN (ESTU, Turkey)
Faruk DİRİSAĞLUK (Eskisehir Osmangazi University)
Barış ERBAŞ (ESTU, Turkey)
Ömer Nezih GEREK (ESTU, Turkey)
Özer GÖK (ESTU, Turkey)
Serdar GÖNCÜ (ESTU, Turkey)
Zerrin AŞAN GREENACRE (ESTU, Turkey)
Cihan KALELİ (ESTU, Turkey)
Gordona KAPLAN (ESTU, Turkey)
T. Hikmet KARAKOÇ (ESTU, Turkey)
Onur KAYA (ESTU, Turkey)
Murat KILIÇ (ESTU, Turkey)
Sabiha KOCA (Eskişehir Osmangazi University, Turkey)
Semra KURAMA (ESTU, Turkey)
Gülbin KURTAY (Ankara University)
Anatoly NİKANOV (Saratov State Technical University, Slovenia)
Murad OMAROV (Kharkiv National University of Radio Electronics, Ukraine)
Emre Aytuğ ÖZSOY (ESTU, Turkey)
Özlem ONAY (ESTU, Turkey)
Gürkan ÖZTÜRK (ESTU, Turkey)
Emrah PEKKAN (ESTU, Turkey)
Najeeb REHMAN (Comsat University, Pakistan)
İsmail Hakkı SARPÜN (Akdeniz University, Turkey)
Sevil SÖYLEYİCİ (Pamukkale University)
Uğur SERİNCAN (ESTU, Turkey)
Cem SEVİK (ESTU, Turkey)
İlkin YÜCEL ŞENGÜN (Ege University, Turkey)
Aynur ŞENSOY ŞORMAN (ESTU, Turkey)
Sevil ŞENTÜRK (ESTU, Turkey)
Engin TIRAŞ (ESTU, Turkey)
Ümran Tezcan ÜN (ESTU, Turkey)
Önder TURAN (ESTU, Turkey)
Osman TUTAL (ESTU, Turkey)
Muammer TÜN (ESTU, Turkey)
Gülay ÜNAL (ESTU, Turkey)
Gülgün YILMAZ ÜNAL (ESTU, Turkey)

Secretary/Typset

Handan YİĞİT

ESKİŞEHİR TECHNICAL UNIVERSITY JOURNAL OF SCIENCE AND TECHNOLOGY
A- Applied Sciences and Engineering
Eskişehir Teknik Üniversitesi Bilim ve Teknoloji Dergisi A – Uygulamalı Bilimler ve Mühendislik

ABOUT

Eskişehir Technical University Journal of Science and Technology A - Applied Sciences and Engineering (ESTUJST-A) is a peer-reviewed and refereed international journal published by Eskişehir Technical University. Since 2000, it has been regularly published and distributed biannually and it has been published quarterly and only electronically since 2016.

The journal accepts only manuscripts written in English.

The journal issues are published electronically in **MARCH, JUNE, SEPTEMBER**, and **DECEMBER.**

AIM AND SCOPE

Eskişehir Technical University Journal of Science and Technology A - Applied Sciences and Engineering is an international peer-reviewed and refereed journal published by Eskişehir Technical University.

The journal is dedicated to the dissemination of knowledge in applied sciences and engineering disciplines.

The journal aims to publish high quality, original international scientific research articles with specific contributions to the literature in the field of engineering and applied sciences. The journal publishes research papers in the fields of applied science and technology such as Physics, Biology, Mathematics, Statistics, Chemistry and Chemical Engineering, Environmental Sciences and Engineering, Civil Engineering, Earth and Atmospheric Sciences, Electrical and Electronical Engineering, Computer Science and Informatics, Materials Sciences and Engineering, Mechanical Engineering, Mining Engineering, Industrial Engineering, Aeronautics and Astronautics, Pharmaceutical Sciences.

The journal publishes original research articles and special issue articles. All articles are peer-reviewed and the articles that have been evaluated are ensured to meet with researchers as soon as possible.

PEER REVIEW PROCESS

Manuscripts are first reviewed by the editorial board in terms of its its journal's style rules scientific content, ethics and methodological approach. If found appropriate, the manuscript is then send to at least two renown referees by editor. The decision in line with the referees may be an acceptance, a rejection or an invitation to revise and resubmit. Confidential review reports from the referees will be kept in archive. All submission process manage through the online submission systems.

OPEN ACCESS POLICY

This journal provides immediate open access to its content on the principle that making research freely available to the public supports a greater global exchange of knowledge. Copyright notice and type of licence : **CC BY-NC-ND.**

PRICE POLICY

Eskişehir Technical University Journal of Science and Technology A - Journal of Applied Sciences and Engineering is an English, peer-reviewed, scientific, free of charge open-access-based journal. The author is not required to pay any publication fees or article processing charges (APCs) for peer-review administration and management, typesetting, and open-access. Articles also receive Digital Object Identifiers (DOIs) from the CrossRef organization to ensure they are always available.

ETHICAL RULES

You can reach the Ethical Rules in our journal in full detail from the link below:

https://dergipark.org.tr/en/pub/estubtda/policy

AUTHOR GUIDELINES

All manuscripts must be submitted electronically.
You will be guided stepwise through the creation and uploading of the various files. There are no page charges. Papers are accepted for publication on the understanding that they have not been published and are not going to be considered for publication elsewhere. Authors should certify that neither the manuscript nor its main contents have already been published or submitted for publication in another journal. We ask a signed copyright to start the evaluation process. After a manuscript has been submitted, it is not possible for authors to be added or removed or for the order of authors to be changed. If authors do so, their submission will be cancelled.

Manuscripts may be rejected without peer review by the editor-in-chief if they do not comply with the instructions to authors or if they are beyond the scope of the journal. After a manuscript has been accepted for publication, i.e. after referee-recommended revisions are complete, the author will not be permitted to make any changes that constitute departures from the manuscript that was accepted by the editor. Before publication, the galley proofs are always sent to the authors for corrections. Mistakes or omissions that occur due to some negligence on our part during final printing will be rectified in an errata section in a later issue.

This does not include those errors left uncorrected by the author in the galley proof. The use of someone else's ideas or words in their original form or slightly changed without a proper citation is considered plagiarism and will not be tolerated. Even if a citation is given, if quotation marks are not placed around words taken directly from another author's work, the author is still guilty of plagiarism. All manuscripts received are submitted to iThenticateR, a plagiarism checking system, which compares the content of the manuscript with a vast database of web pages and academic publications. In the received iThenticateR report; The similarity rate is expected to be below 25%. Articles higher than this rate will be rejected.

Uploading Articles to the Journal

Authors should prepare and upload 2 separate files while uploading articles to the journal. First, the Author names and institution information should be uploaded so that they can be seen, and then (using the additional file options) a separate file should be uploaded with the Author names and institution information completely closed. When uploading their files with closed author names, they will select the "Show to Referee" option, so that the file whose names are closed can be opened to the referees.

Style and Format
Manuscripts should be **single column** by giving one-spaced with 2.5-cm margins on all sides of the page, in Times New Roman font (font size 11). Every page of the manuscript, including the title page, references, tables, etc., should be numbered. All copies of the manuscript should also have line numbers starting with 1 on each consecutive page.

Manuscripts must be upload as word document (*.doc, *.docx vb.). Please avoid uploading ***texts in *.pdf format.***

Symbols, Units and Abbreviations
Standard abbreviations and units should be used; SI units are recommended. Abbreviations should be defined at first appearance, and their use in the title and abstract should be avoided. Generic names of chemicals should be used. Genus and species names should be typed in italic or, if this is not available, underlined.

Manuscript Content
Articles should be divided into logically ordered and numbered sections. Principal sections should be numbered consecutively with Arabic numerals (1. Introduction, 2. Formulation of problem, etc.) and subsections should be numbered 1.1., 1.2., etc. Do not number the Acknowledgements or References sections. The text of articles should be, if possible, divided into the following sections: Introduction, Materials and Methods (or Experimental), Results, Discussion, and Conclusion.

Title and contact information
The first page should contain the full title in sentence case (e.g., Hybrid feature selection for text classification), the full names (last names fully capitalised) and affiliations (in English) of all authors (Department, Faculty, University, City, Country, E-mail), and the contact e-mail address for the clearly identified corresponding author. The first page should contain the full title, abstract and keywords (both English and Turkish).

Abstract
The abstract should provide clear information about the research and the results obtained, and should not exceed 300 words. The abstract should not contain citations and must be written in Times New Roman font with font size 9.

Keywords
Please provide 3 to 5 keywords which can be used for indexing purposes.

Introduction
The motivation or purpose of your research should appear in the "Introduction", where you state the questions you sought to answer, and then provide some of the historical basis for those questions.

Methods
Provide sufficient information to allow someone to repeat your work. A clear description of your experimental design, sampling procedures, and statistical procedures is especially important in papers describing field studies, simulations, or experiments. If you list a product (e.g., animal food, analytical device), supply the name and location of the manufacturer. Give the model number for equipment used.

Results
Results should be stated concisely and without interpretation.

Discussion
Focus on the rigorously supported aspects of your study. Carefully differentiate the results of your study from data obtained from other sources. Interpret your results, relate them to the results of previous research, and discuss the implications of your results or interpretations.

Conclusion
This should state clearly the main conclusions of the research and give a clear explanation of their importance and relevance. Summary illustrations may be included.

Acknowledgments
Acknowledgments of people, grants, funds, etc. should be placed in a separate section before the reference list. The names of funding organizations should be written in full.

References
AMA Style should be used in the reference writing of our journal. If necessary, at this point, the reference writings of the articles published in our article can be examined.

Citations in the text should be identified by numbers in square brackets. The list of references at the end of the paper should be given in order of their first appearance in the text. All authors should be included in reference lists unless there are 10 or more, in which case only the first 10 should be given, followed by 'et al.'. Do not use individual sets of square brackets for citation numbers that appear together, e.g., [2,3,5–9], not [2], [3], [5]–[9]. Do not include personal communications, unpublished data, websites, or other unpublished materials as references, although such material may be inserted (in parentheses) in the text. In the case of publications in languages other than English, the published English title should be provided if one exists, with an annotation such as "(article in Turkish with an abstract in English)". If the publication was not published with an English title, cite the original title only; do not provide a self-translation. References should be formatted as follows (please note the punctuation and capitalisation):

Journal articles
Journal titles should be abbreviated according to ISI Web of Science abbreviations.
Guyon I, Elisseeff A. An introduction to variable and feature selection. J Mach Learn Res 2003; 3: 1157-1182.

Izadpanahi S, Ozcınar C, Anbarjafari G, Demirel H. Resolution enhancement of video sequences by using discrete wavelet transform and illumination compensation. Turk J Elec Eng & Comp Sci 2012; 20: 1268-1276.

Books
Haupt RL, Haupt SE. Practical Genetic Algorithms. 2nd ed. New York, NY, USA: Wiley, 2004.
Kennedy J, Eberhart R. Swarm Intelligence. San Diego, CA, USA: Academic Press, 2001.

Chapters in books
Poore JH, Lin L, Eschbach R, Bauer T. Automated statistical testing for embedded systems. In: Zander J, Schieferdecker I, Mosterman PJ, editors. Model-Based Testing for Embedded Systems. Boca Raton, FL, USA: CRC Press, 2012. pp. 111-146.

Conference proceedings
Li RTH, Chung SH. Digital boundary controller for single-phase grid-connected CSI. In: IEEE 2008 Power Electronics Specialists Conference; 15–19 June 2008; Rhodes, Greece. New York, NY, USA: IEEE. pp. 4562-4568.

Theses
Boynukalın Z. Emotion analysis of Turkish texts by using machine learning methods. MSc, Middle East Technical University, Ankara, Turkey, 2012.

Tables and Figures
All illustrations (photographs, drawings, graphs, etc.), not including tables, must be labelled "Figure." Figures must be submitted in the manuscript.

All tables and figures must have a caption and/or legend and be numbered (e.g., Table 1, Figure 2), unless there is only one table or figure, in which case it should be labelled "Table" or "Figure" with no numbering. Captions must be written in sentence case (e.g., Macroscopic appearance of the samples.). The font used in the figures should be Times New Roman. If symbols such as ×, μ, η, or ν are used, they should be added using the Symbols menu of Word.

All tables and figures must be numbered consecutively as they are referred to in the text. Please refer to tables and figures with capitalisation and unabbreviated (e.g., "As shown in Figure 2…", and not "Fig. 2" or "figure 2").

The resolution of images should not be less than 118 pixels/cm when width is set to 16 cm. Images must be scanned at 1200 dpi resolution and submitted in jpeg or tiff format. Graphs and diagrams must be drawn with a line weight between 0.5 and 1 point. Graphs and diagrams with a line weight of less than 0.5 point or more than 1 point are not accepted. Scanned or photocopied graphs and diagrams are not accepted.

Figures that are charts, diagrams, or drawings must be submitted in a modifiable format, i.e. our graphics personnel should be able to modify them. Therefore, if the program with which the figure is drawn has a "save as" option, it must be saved as *.ai or *.pdf. If the "save as" option does not include these extensions, the figure must be copied and pasted into a blank Microsoft Word document as an editable object. It must not be pasted as an image file (tiff, jpeg, or eps) unless it is a photograph.

Tables and figures, including caption, title, column heads, and footnotes, must not exceed 16 × 20 cm and should be no smaller than 8 cm in width. For all tables, please use Word's "Create Table" feature, with no tabbed text or tables created with spaces and drawn lines. Please do not duplicate information that is already presented in the figures.

Article Corrections and Uploading to the System
Authors should upload the desired edits for their articles without destroying or changing the Template file of the article, by selecting and specifying the relevant edits as Colored, and also submit the Clean version of the article in 2 separate files (using the Additional file option if necessary). * In case of submitting a corrected article, a separate File in Reply to the Referees must be prepared and the "Reply to the Referees" option in the Add additional file option should be checked and uploaded. If a separate file is not prepared in response to the referees, the Author

will definitely be asked to upload the relevant file again and the evaluation will be in the pending phase.

CONFLICT OF INTEREST STATEMENT

The authors are obliged to present the conflict of interest statement at the end of the article.

ESKİŞEHİR TECHNICAL UNIVERSITY JOURNAL OF SCIENCE AND TECHNOLOGY
A – Applied Sciences and Engineering
Volume: 23 / Number: 3 / September - 2022

CONTENTS

RESEARCH ARTICLE

ESKİŞEHİR TECHNICAL UNIVERSITY JOURNAL OF SCIENCE AND TECHNOLOGY
A- APPLIED SCIENCES AND ENGINEERING

2022, 23(3), pp. 195-206, DOI:10.18038/estubtda.975913

RESEARCH ARTICLE

ANALYSIS OF THE COLLISION EFFECT FOR ADJACENT STRUCTURES IN THE TIME-FREQUENCY DOMAIN

Ömer Fatih SAK [1,*] and Kemal BEYEN [2]

[1] Civil Engineering Department, Engineering Faculty, Doğuş University, İstanbul, Turkey
[2] Civil Engineering Department, Engineering Faculty, Kocaeli University, Kocaeli, Turkey

ABSTRACT

Many reinforced concrete structures are built side by side in our cities. There are very few applications of earthquake joints in adjacent apartment buildings, most of them were constructed completely adjacent. Adjoining buildings or any property should be protected from damage or collapse during construction, restoration and demolition work. In case of the static condition, protection must be supplied for foundations, walls and roofs. We have already observed many building collapses in Turkey with a great number of life lost. For the constructed buildings, there is a need to understand the structural system of an existing building to manage risk. In case of earthquakes like dynamic loading, earthquake joints are essential. The Turkish Building Earthquake Code (TBEC) 2018 requires calculations of vertical joints for some types of structures. Earthquake joints should be left in the gap calculated for structures of some height. It is thought that this gap will prevent the structures from colliding. However, it has been the subject of research how the performance of the building will change when it is produced adjacent or when floor offsets cause collisions at earthquake joints. In this study, structures of different heights were analyzed in the time domain for specific earthquake motions. Collision situations of more than two buildings are discussed by making a street model. Structural performances of discrete and adjacent structures obtained from nonlinear analysis were compared. The motion parameters obtained from the structures were analyzed in the time-frequency domain by wavelet and Hilbert transforms. To determine the effects of earthquake joints, condition assessment and damage detection studies were carried out and the sufficiency of seismic joints was discussed.

Keywords: Adjacent structures, Collision impact, Vertical seismic joints, Wavelet transform, Hilbert Huang Transform

1. INTRODUCTION

In the section related to earthquake joints in the Turkish earthquake code, it is stated that vertical earthquake joints should be placed at certain distances between adjacent structures built depending on the height. The minimum joint space to be left in by article 2.10.3.2 will be at least 30 mm up to 6 m height and at least 10 mm will be added to this value for every 3 m height after 6 m. While these joints were left in the structures built after the earthquake, many existing structures were built completely adjacent to each other before the earthquake. It has been a subject of research how the structural behaviors change if the floor displacements cross the earthquake joints and cause collisions as a result of the oscillations in opposite directions at the same time in such adjacent buildings or buildings with different periods. The adequacy of earthquake joints and the behavior of fully adjacent structures were investigated by nonlinear analysis in the time domain under the effect of the eleven earthquake recordings through the analytical model. Changes in structural performances are compared when the building is separate and adjacent. Results were analyzed in time-frequency domain by wavelet analysis and the Hilbert Huang transform method.

The main study on collision in adjacent buildings was carried out by Anagnostopoulos [1]. In the analysis, structures are modeled with single degree of freedom systems and collisions are simulated with the help of a linear viscoelastic model of impact force. Multi-degree of freedom (MDOF) models, with the mass of each floor collected at the floor level, are used to analyze in more detail the earthquake-

*Corresponding Author: osak@dogus.edu.tr
Received: 29.07.2021 Published: 27.09.2022

related collision in buildings of different heights. Among analytical analyzes, collisions are modeled as nonlinear impact between a single degree of freedom oscillator and a rigid barrier based on the nonlinear Hertz collision model used by Davis [2]. Taking the collision effect into account in the nonlinear field gives more realistic results in calculations. Maison and Kasai [3] established the equation of degrees of freedom of movement for different structure collisions. With this theory, he studied the behavioral characteristics of a 15-story building in the computer environment. Filiatrault et al. [4] conducted vibration table tests for collisions between adjacent three and eight-story steel frames in the time history of the 1940 El-Centro earthquake and the experimental results were compared with the predictions given by the two computer programs. Papadrakakis and Mouzakis [5,6], by subjecting to sinusoidal and random movements, conducted shake table experiments for collision between two-storey reinforced concrete buildings with zero spacing and their experimental results were compared with the estimates made by the Lagrange multiplier method.

Other approaches have been proposed to determine the relative displacement between two structures during earthquakes. For example, Stavroulakis and Abdalla [7] used the pseudo-static method, Filiatrault and Cervantes [8] used nonlinear time history analysis, and Lin [9] proposed the stochastic method of random vibration. Despite all these differences in ideas, there is consensus that current building code provisions for seismic collision are very protective. The spatial ground motion effect on impacts was evaluated by Jeng and Kasai [10] and Hao and Zhang [11]. In most of these studies, a shock absorber spring model with linear stiffness or bilinear stiffness was used to model the impact force between buildings. However, the actual impact forces between structures or between various components of a structure are generally not linear. Pantelides and Ma [12] examined the collisions between a single degree of freedom and damped structure and a rigid obstacle with ground motions of the 1940 El Centro, 1971 San Fernando, 1989 Loma Prieta and 1994 Northridge earthquakes. Chau and Wei [13] examined nonlinear collisions between two single degrees of freedom oscillators. Rahman et al. [14] examined the collision of two 12-storey and 6-storey buildings with different dynamic properties, considering the ground properties. Muthukumar [15] revealed that in the 1999 Kocaeli earthquake, a six-storey building in Gölcük collided with the neighboring two-storey building, and the column on the third floor of the six-storey building was severely damaged and the two-storey building collapsed due to shear forces. Gong and Hao [16] analyzed the torsional effects between symmetrical and non-symmetrical systems that are subjected to bidirectional ground motion. Wang and Chau [17] modeled the torsional collision between two unsymmetrical buildings using the nonlinear Hertz model technique. As a result of the studies, he stated that the torsion effect is generally complex compared to the translational effect. Jankowski [18] studied a detailed three-dimensional pounding response analysis of Olive View Hospital main building using the finite element method (FEM) with nonlinear model material behavior with stiffness degradation of concrete during the San Fernando earthquake in 1971. Pant et al. [19] presented a three-dimensional simulation of seismic collisions between reinforced concrete moment-resistant frame buildings, considering the material and geometric nonlinear structures. Çetinkaya [20] analyzed the collision of two neighboring buildings with different stiffness for 4 different spring models and compared the results. He concluded that the model in which the interaction between buildings is seen most clearly is the Hertz (nonlinear elastic spring) model. Mahmoud et al. [21] examined the impact of soil elasticity on these two structures as well as the collision of two non-linear structures of equal height under the effect of an earthquake. As a result of the analysis, it has been observed that the cyclic and horizontal movements of the ground affect the collision of two buildings. Mate et al. [22] presented a comparative study of various existing linear and nonlinear simulation models for collision in three adjacent single degrees of freedom and multi-degree of freedom linear elastic structures. This study showed that the impact result depends on the ground motion characteristics and the relationship between the first periods in buildings. Akköse and Sunca [23] evaluated the seismic performance of a train station building in the 2011 Van earthquake by nonlinear time history analysis and the results have been compared with and without pounding effects. Beyen [24] stated that the results of building diagnosis can contribute to the situation analysis of existing structures in structural health checks after an important earthquake. Updating analytical building models and identifying them by the facts are important for

determining the post-earthquake situation in adjacent structures. Kamal and Inel [25] investigated the effects of pounding on seismic behavior of 5, 8, 10, 13 and 15 storey RC buildings and showed that significant changes may occur in the building displacement demands due to the collision of the mid-rise RC neighboring buildings with the insufficient seismic gap. As a result of the study, the displacement factor for medium-rise RC buildings was proposed. Cayci and Akpinar [26] evaluated pounding effects on typical building structures considering soil-structure interaction. They studied nonlinear time history analysis of 4, 8, 12 and 16 story buildings with 15 different ground motions and they showed that the minimum distance required to avoid collision seems not to be sufficient.

2. COLLISION MODEL

In this model, to represent the relationship between the force of impact and displacement, the Hertz law of contact has been utilized. Nonlinear elastic spring is activated by closing the space (d) between buildings. The collision force is represented by u (t) = u_i (t) - u_j (t) as follows;

$$F_C = k_G[u(t) - d]^{3/2} \quad u(t) - d > 0 \quad (collision\ situation) \tag{2a}$$

$$F_C = 0 \quad u(t) - d \leq 0 \quad (noncollision\ situation) \tag{2b}$$

Here; ui (t) and uj (t) are the relative displacements of neighboring buildings in the same direction, d represents the space between two buildings, k_G is the nonlinear elastic spring constant, F_c is the impact force. The mass density ρ and radius R_i approximation of colliding structures can be found from the equation below. [Goldsmith (1960)]:

$$R_i = \sqrt{\frac{3m_i}{4\pi\rho}}\,, \qquad i = 1,2 \tag{2c}$$

Nonlinear spring tension k_h depends on the material properties and radii of colliding structures according to the formula: where h_1 and h_2 are the material parameters defined by the formula:

$$k_h = \frac{4}{3\pi(h_1 + h_2)}\left[\frac{R_1 R_2}{R_1 + R_2}\right]^{1/2} \tag{2d}$$

$$h_i = \frac{1 - \gamma_i}{\pi E_i} \quad i = 1,2 \tag{2e}$$

Here, γ_i and E_i are the Poisson's ratio and the modulus of elasticity, respectively. The coefficient K_h depends on the material properties and geometry of the colliding objects.
As the structural strength in the calculation, the bulk density is taken as ρ = 2500 kg/m^3, Poisson's ratio γ_i = 0.2, elasticity modulus $E_i = 2.8\text{x}10^{10}$ N/m^2 and $k_G = 1.13\text{x}10^9$ N/m$^{3/2}$ for concrete to concrete impacts based on numerical simulation suggested by Jankowski [27].

3. ANALYTICAL STUDIES

Four, five and six-storey structures were modeled in accordance with TS500 [28] and TBEC (2018) [29], the columns were selected as 30x60 cm^2, and the beams as 25x50 cm^2 with C25/30 class concrete. The effective section stiffness is 0.7 for columns and 0.35 for beams. Spans in *x* and *y* directions in plan are selected as 3m and the floor height is 3m as shown in Figure 1. Analytical structures according to the earthquake specifications, the earthquake joints were located completely adjacent and singular. With the 11 earthquake recordings, numerical model was analyzed in a nonlinear fashion in the time domain and damage parameters were determined. Damage detection was performed using the wavelet transform and Hilbert Huang transform, based on deformation distributions in the joints and acceleration records obtained through the structural observation points. In addition, the columns connected to the foundation

in the structure were modeled as built-in and fixed support and changes in the distribution of damage were also observed for the same earthquake loading.

First fundamental period of the structure, soft story, weak story, torsional irregularity check, limitations of relative story drifts and second order effects were performed in accordance with TBEC (2018) [29] and the results were acceptable laying in the appropriate ranges. The modal parameters of the structure were determined by using modal analysis approach within the finite element package.

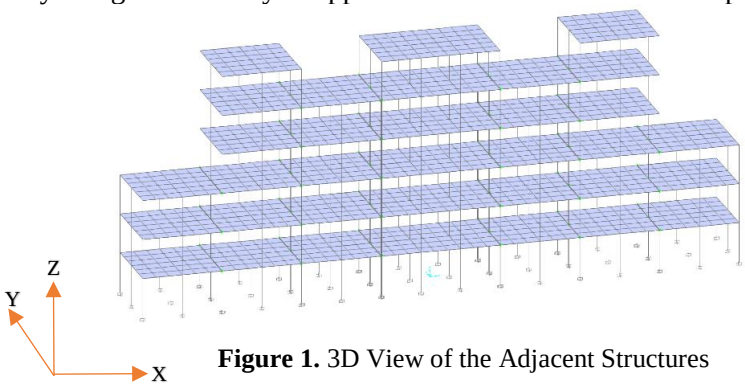

Figure 1. 3D View of the Adjacent Structures

3.1. Determination of Earthquake Performance of The Adjacent Buildings by Applying Nonlinear Method for A Series of Earthquake Recordings.

Results of the nonlinear case tabulated and plotted in Figures 1 and 2 were obtained for the identified modal parameters of the structural system by the SAP2000 package for the strong earthquake loading. As an acceleration record, 11 different earthquakes from different recording stations were scaled and used including the data of the Yarımca station recorded during Kocaeli earthquake 1999. The earthquake archive of this study is listed, and their spectral graphs are shown in Figure 2.

Result ID	Spectral Ordinate	Record Seq. #	MSE	Scale Factor	Tp(s)	D5-75(s)	D5-95(s)	Arias Intensity (m/s)	Event	Year	Station	Mag	Mechanism
1	SRSS	6	0.0926	1.4294	-	17.7	24.2	1.6	Imperial Valley-02	1940	El Centro Array #9	6.95	strike slip
2	SRSS	15	0.0583	2.3195	-	10.7	30.3	0.6	Kern County	1952	Taft Lincoln School	7.36	Reverse
3	SRSS	20	0.2862	1.8676	-	6.8	19.4	0.5	Northern Calif-03	1954	Ferndale City Hall	6.5	strike slip
4	SRSS	30	0.2584	1.9328	-	2.4	7.5	0.9	Parkfield	1966	Cholame - Shandon Array #5	6.19	strike slip
5	SRSS	36	0.3868	2.8865	-	25.0	49.3	0.2	Borrego Mtn	1968	El Centro Array #9	6.63	strike slip
6	SRSS	57	0.8564	2.9471	-	10.6	16.8	1.0	San Fernando	1971	Castaic - Old Ridge Route	6.61	Reverse
7	SRSS	95	0.3937	1.5033	-	4.9	10.6	2.0	Managua, Nicaragua-01	1972	Managua, ESSO	6.24	strike slip
8	SRSS	125	0.4961	2.0327	-	2.5	4.9	1.2	Friuli, Italy-01	1976	Tolmezzo	6.5	Reverse
9	SRSS	126	0.0789	0.6988	-	5.6	7.0	5.7	Gazli, USSR	1976	Karakyr	6.8	Reverse
10	SRSS	138	0.1395	2.8759	-	14.6	19.5	0.3	Tabas, Iran	1978	Boshrooyeh	7.35	Reverse
11	SRSS	1176	0.4872	0.8834	4.949	7.0	15.1	1.3	Kocaeli, Turkey	1999	Yarimca	7.51	strike slip

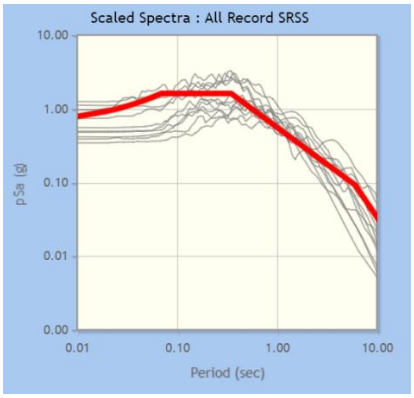

Figure 2. Earthquake Acceleration Records and Spectral Graphs (Peer Ground Motion Database)

Table 1. Undamaged (Modal) and damaged (Modal-NL) Jointed Structure Parameters

OUTPUTCASE	STEP TYPE	STEP NUM	PERIOD	FREQUENCY	CIRC FREQ	EIGENVALUE
			Sec	Cyc/sec	rad/sec	rad2/sec2
MODAL	Mod	1	0.707	1.414	8.887	78.973
MODAL	Mod	2	0.690	1.450	9.111	83.003
MODAL	Mod	3	0.690	1.450	9.111	83.003
MODAL	Mod	4	0.571	1.751	11.002	121.049
MODAL-NL	Mod	1	0.711	1.406	8.837	78.088
MODAL-NL	Mod	2	0.693	1.442	9.062	82.117
MODAL-NL	Mod	3	0.693	1.442	9.063	82.144
MODAL-NL	Mod	4	0.574	1.743	10.954	120.001

In Table 1 the period of the first mode for the *x* direction is slightly increased for the undamaged model from 0.707 sec to 0.711 sec in case of the damage.

When the plastic hinges of the columns in the structure were examined, in Figure 3 it was observed that several elements surpassed the collapse prevention performance level to one step ahead collapse at the first floor. The reference parameters of the study model are assigned based on TBEC (2018) values and lumped plasticity approach has been adopted.

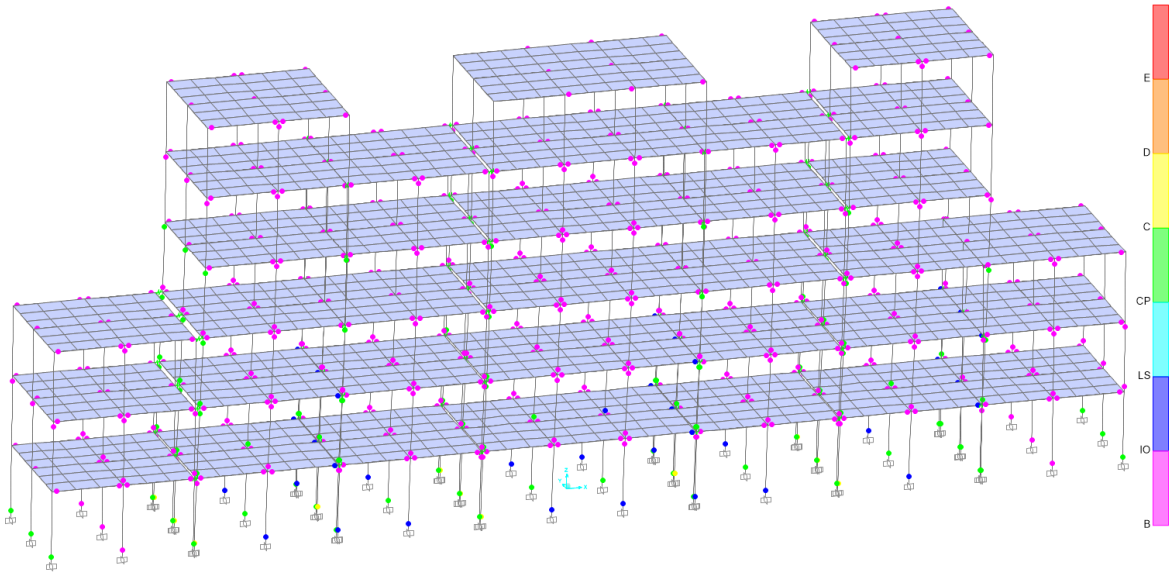

Figure 3. Plastic Hinges Graph for Joint Structures. Result of the Joint Conditions in case of the Strongest Earthquake (IO: Immediate Occupancy, LS: Life Safety, CP: Collapse Prevention, C: Collapse)

The period of the dominant mode for the *x* direction increased from 0.707 sec in the undamaged model to 0.711 sec in the damaged model. The frequency change in the discrete structure is lower than in the joint structure. Looking at the order of damage, it is seen that from Figure 4 the level of performance in structural elements does not change significantly. From such a result, it can be concluded that the adjacent spans of the earthquake joints proposed in the earthquake regulation is sufficient for the structural system.

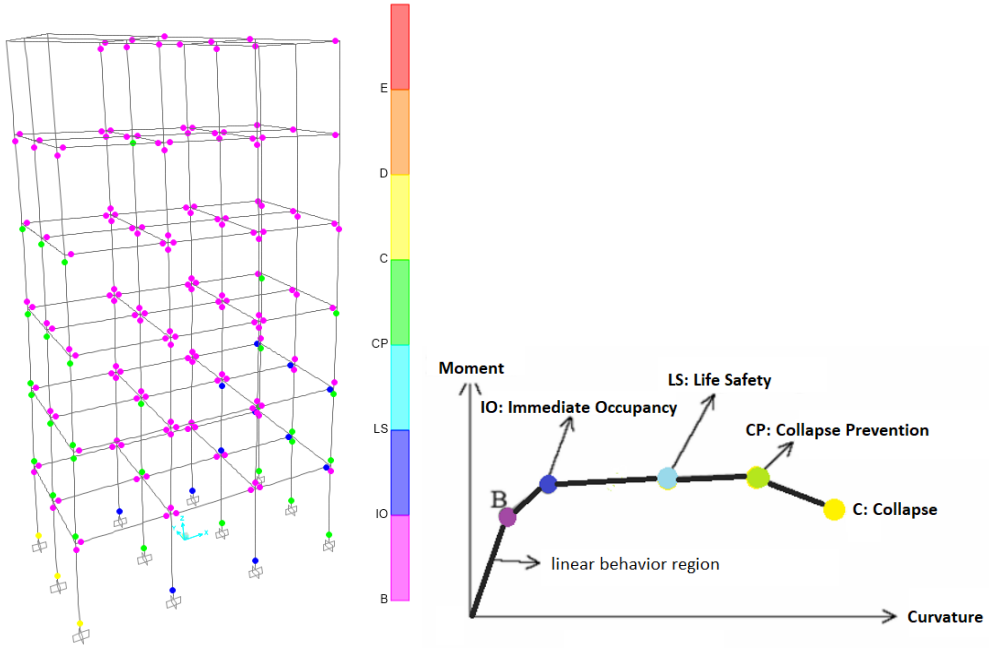

Figure 4. Plastic Hinges Graph for Single Structure Result of Analysis in case of the Strongest Earthquake.

Table 2. Undamaged (Modal) and Damaged (Modal-NL) Single Structure Parameters

OUTPUT CASE	STEP TYPE	STEP NUM	PERIOD	FREQUENCY	CIRC FREQ	EIGENVALUE
			Sec	Cyc/sec	rad/sec	rad2/sec2
MODAL	Mod	1	0.707	1.414	8.887	78.973
MODAL	Mod	2	0.521	1.920	12.066	145.591
MODAL	Mod	3	0.512	1.951	12.260	150.307
MODAL	Mod	4	0.231	4.334	27.233	741.660
MODAL-NL	Mod	1	0.711	1.406	8.837	78.088
MODAL-NL	Mod	2	0.522	1.915	12.031	144.750
MODAL-NL	Mod	3	0.514	1.944	12.214	149.170
MODAL-NL	Mod	4	0.232	4.318	27.131	736.094

When we consider the structure that is insufficient according to the regulation by taking the earthquake joint 1 cm, the structure is damaged at an advanced level in the face of the same earthquake forces in Figure 5 and Figure 6. It is understood that the distances specified in the regulation are sufficient and necessary when compared with the structure where sufficient adjacent spans are not applied.

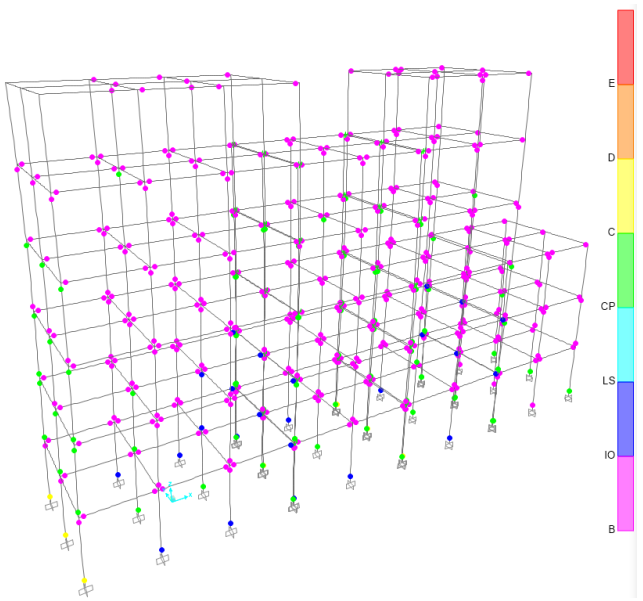

Figure 5. Plastic Hinge Graph for Structures Constructed with Sufficient Adjacent Spans. Result of Analysis in case of the Strongest Earthquake.

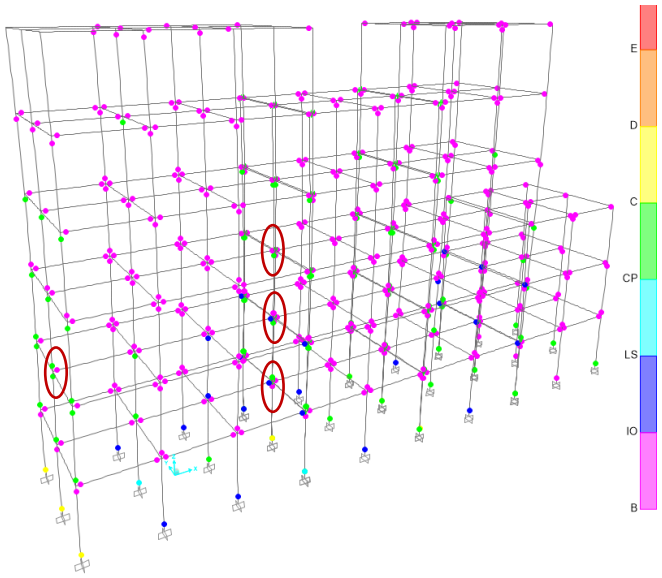

Figure 6. Plastic Hinge Graph for Structures that don't have Enough Adjacent Spans. Result of Analysis for the Strongest Earthquake.

Especially when the first structure is considered, damage levels that reaches to the collapse prevention zone are observed marked in Figure 6. From the structures left with insufficient joints, the columns in the structure adjacent to the first building are increased from 30x60 cm^2 to 100x100 cm^2, resulting in a similar distribution of damage when looking at the interaction of the rigid structure.

The rigidity of the building adjacent to the structure, where the joint gap is insufficient as seen in Figure 7, somewhat reduces the damage levels, but as a result, structural performance levels cannot reach the predicted levels. Column shear force increases from 152.45 kN to 161.71 kN in the structure where there is not enough space. The base shear force increases from 361.05 kN to 372.85 kN. As a result, the column shear forces observed in the collision increased by approximately 6%, and the base shear force increased by 3%.

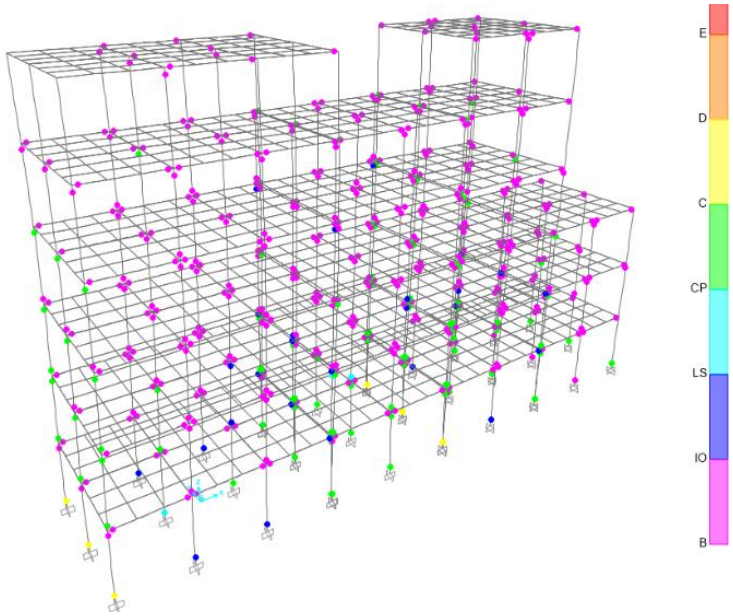

Figure 7. Hinge Graph for a Rigid Neighboring Structures That don't have Enough Adjacent Spans. Result of Analysis for the Strongest Earthquake Case

3.2. Damage Diagnostic Work by Wavelet Analysis Method Over Damaged and Undamaged Parameters

The damage is mainly concentrated in columns as seen in Figure 7. For discrete time-frequency changes in operational modal parameters, discrete Daubechies (Db4), Morlet, Mexican Hat, and Symlet wavelet filters were tested to detect the damage by examining the differences between the two conditions. Details of the theory and implementation of Time-Frequency analysis can be found in following studies Sak and Beyen, Beyen [30, 31, 32]. The necessary codes for this are written in MATLAB. As a result of the analysis, Db4 wavelet models were found to be suitable and sufficient for the analysis of the structures. Here, based on the damaged and undamaged records of one of the damaged elements, we look at the noticeable differences in the wavelet and Hilbert Huang transformation.

As can be seen from the graphs in Figure 8, the frequency order changes in the wavelet spectra at the time of damage formation. And in the Figure 9 Hilbert Huang transformation, the frequency change of the undamaged element is significant, while in the damaged element it changes depending on time.

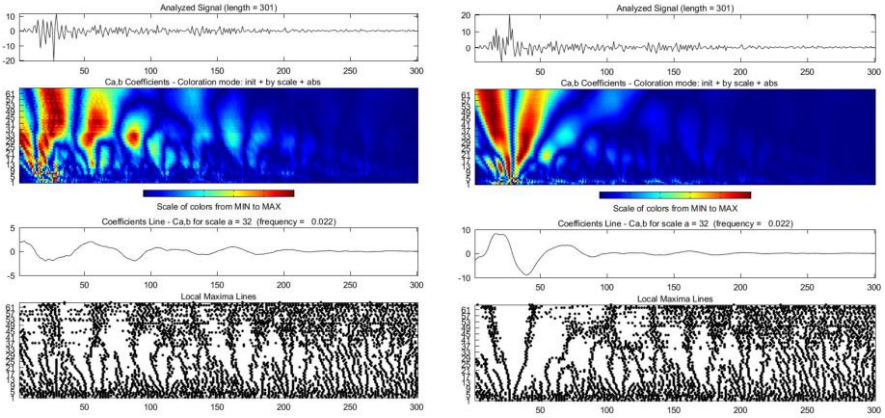

Figure 8. Wavelet Transformation of an Element Undamaged (left) and Damaged (Right) for an intensive Earthquake

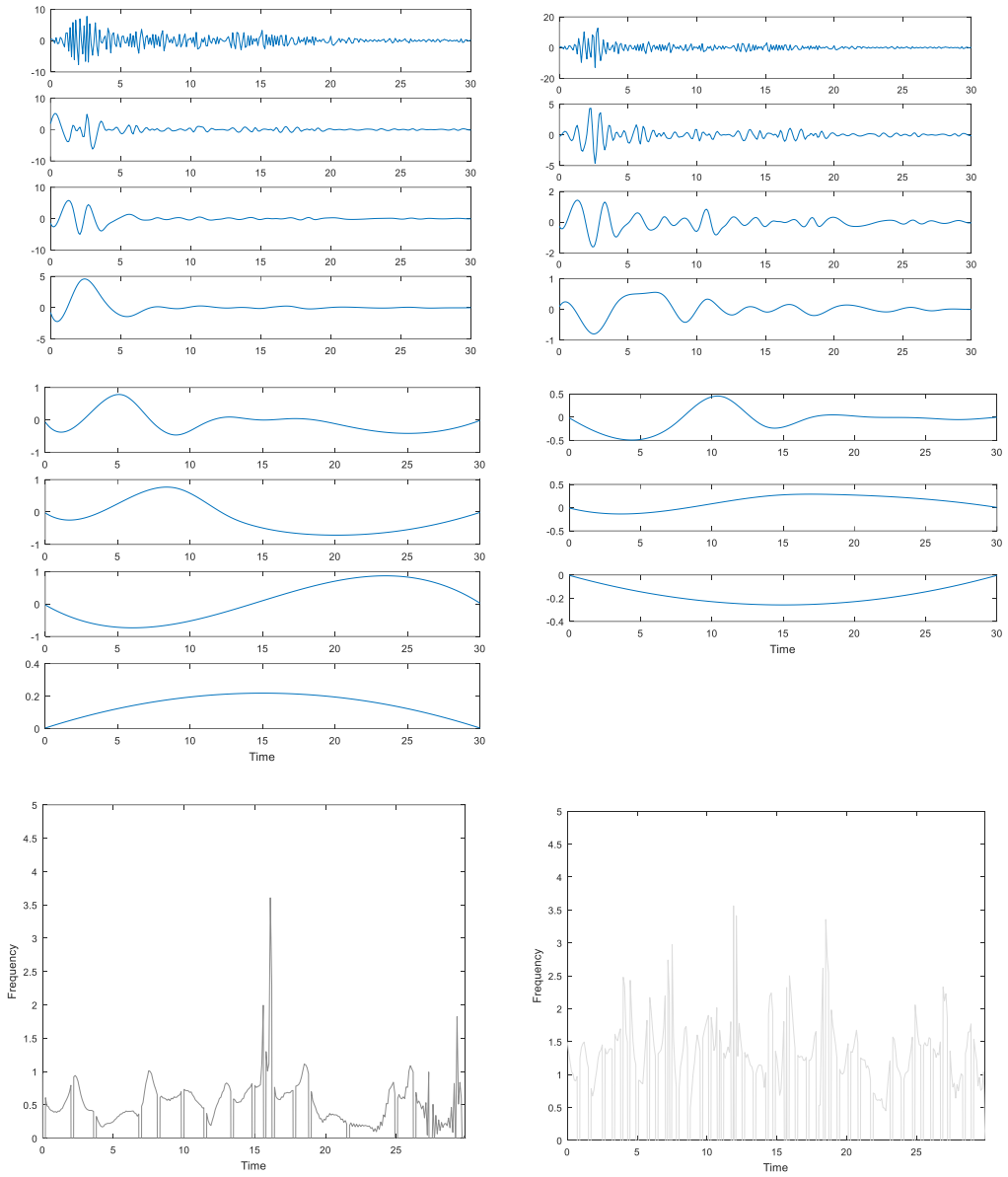

Figure 9. Hilbert Huang Transformation of Undamaged (Left) and Damaged (Right) Elements

4. RESULT

As revealed in this study, the vertical earthquake joints determined in TBEC (2018) [29] are necessary and sufficient for adjacent structures. In structures where earthquake joints are not applied, structural performance levels cannot be encountered. In adjacent buildings, each building's rigidity in line reduces structural damage to some extent, but the target performance level cannot be reached. For this reason, leaving vertical earthquake joints in the adjacent span determined in the regulation significantly affects the earthquake performance of the buildings.

Damage detection with a wavelet and Hilbert Huang transforms can be used as effective methods in structural health monitoring autonomous systems. Damaged elements and undamaged elements can be detected based on the frequency content that changes over time in the spectra.

In the earthquake regulation that will be updated in future, structural health monitoring strategies can be used, which give high resolution in the time-frequency domain as declared in this study.

CONFLICT OF INTEREST

The authors stated that there are no conflicts of interest regarding the publication of this article.

REFERENCES

[1] Anagnostopoulos SA. Pounding of buildings in series during earthquakes. Earthquake Engineering and Structural Dynamics 1988; 16: 443-456.

[2] Davis RO. Pounding of buildings modelled by an impact oscillator. Earthquake Engineering and Structural Dynamics 1992; 21: 253–274.

[3] Maison B, Kasai K. Dynamics of pounding when two building collide. Earthquake Engineering and Structural Dynamics 1992; 21: 771-786.

[4] Filiatrault A, Wagner P, Cherry S. Analytical prediction of experimental building pounding. Earthquake Engineering and Structural Dynamics 1995; 24: 1131–1154.

[5] Papadrakakis M, Mouzakis H. Earthquake simulator testing of pounding between adjacent buildings. Earthquake Engineering and Structural Dynamics 1995; 24: 811–834.

[6] Papadrakakis M, Apostolopoulou C, Zacharopoulos A, Bitzarakis S. Three-dimensional simulation of structural pounding during earthquakes. Journal of Engineering Mechanics 1996; 122: 423–431.

[7] Stavroulakis GE, Abdalla KM. Contact between adjacent structures. Journal of Structural Engineering 1991; 117: 2838–2850.

[8] Filiatrault A, Cervantes M. Separation between buildings to avoid pounding during earthquakes. Canadian Journal of Civil Engineering 1995; 22: 164–179.

[9] Lin JH. Separation distance to avoid seismic pounding of adjacent buildings. Earthquake Engineering and Structural Dynamics 1997; 26: 395–403.

[10] Jeng V, Kasai K. Spectral relative motion of two structures due to seismic travel waves. Journal of Structural Engineering 1996; 122: 1128–1135.

[11] Hao H, Zhang SR. Spatial ground motion effect on relative displacement of adjacent building structures. Earthquake Engineering and Structural Dynamics 1999; 28: 333–349.

[12] Pantelides CP, Ma X. Linear and non-linear pounding of structural systems. Computers and Structures 1998; 66: 79–92.

[13] Chau KT, Wei XX. Pounding of structures modelled as non-linear impacts of two oscillators. Earthquake Engineering and Structural Dynamics 2000; 30: 633–651.

[14] Rahman AM, Carr AJ, Moss PJ. Seismic pounding of a case of adjacent multiplestorey buildings of differing total heights considering soil flexibility effects. Bull NZ Soc Earthquake Eng 2001; 34: 140–159.

[15] Muthukumar S. A contact element approach with hysteresis damping for the analysis and design of pounding in bridges. In partial fulfillment of the requirements for the degree of doctor of

philosophy in civil and environmental engineering, Georgia Institute of Technology, Georgia, 2003.

[16] Gong L, Hao H. Analysis of coupled lateral-torsional-pounding responses of one storey asymmetric adjacent structures subjected to bi-directional ground motions Part I: Uniform ground motion input. Advances in Structural Engineering 2005; 8(5): 463-479.

[17] Wang LX, Chau KT. Chaotic Seismic Torsional Pounding between two Single story Asymmetric Towers. The 14th World Conference on Earthquake Engineering, Beijing, China, 2008.

[18] Jankowski R. Non-linear FEM analysis of earthquake-induced pounding between the main building and the stairway tower of the Olive View Hospital. Engineering Structures 2009; 31: 1851-1864.

[19] Pant R, Wijeyewickrema AC. Seismic pounding between reinforced concrete buildings: A study using recently proposed contact element models. Proc. of Fourteenth European Conference on Earthquake Engineering, Ohird, Republic of Macedonia, 2010.

[20] Çetinkaya G. Deprem Yer Hareketine Maruz Komşu Binalarda Çarpışma Analizi (Pounding analysis of adjacent buildings to earthquake ground motion). Master's thesis, Karadeniz Technical University, Trabzon, Türkiye. 2011.

[21] Mahmoud S, Elhamed AA, Jankowski R. Earthquake-induced pounding between equal height multi-storey buildings considering soil-structure interaction. Bulletin of Earthquake Engineering 2013; 11: 1021-1048.

[22] Mate N U, Bakre SV, Jaiswal OR. Comparative Study of Impact Simulation Models for Linear Elastic Structures in Seismic Pounding. The 15th World Conference on Earthquake Engineering, Lisbon, Portugal, 2012.

[23] Akköse M, Sunca F. Seismic performance evaluation of a train station building considering earthquake-induced pounding effects. Symposium on Innovate Technologies in Engineering and Science, Antalya, Türkiye. 2016.

[24] Beyen K. Titreşim verisiyle güncellenmiş sonlu eleman modeliyle hasar simulasyonu (Damage simulation by finite element updating using vibration characteristics). 10.17341/gazimmfd.322165, Journal of the Faculty of Engineering and Architecture of Gazi University 2017; 32(2): 403-415.

[25] Kamal M, Inel M. Effects of pounding on displacement demands in mid-rise RC buildings. Pamukkale University Journal of Engineering Sciences 2021; 27(6): 703-710.

[26] Cayci BT, Akpinar M. Seismic pounding effects on typical building structures considering soil-structure interaction. Structures 2021; 34: 1858-1871.

[27] Jankowski R. Non-Linear Viscoelastic Modeling of Earthquake-Induced Structural Pounding. Earthquake Engineering and Structural Dynamics 2005; 34: 595-611.

[28] Design and Construction Rules of Reinforced Concrete Structures, Turkish Standard (TS) 500, Turkish Standards Institute, Ankara, 2000.

[29] Türkiye Building Earthquake Code (TBEC) 2018, Disaster and Emergency Management Presidency, Ankara, Türkiye, 2018.

[30] Beyen K. Dalgacık spektrumlarının yapı sağlığı durum değerlendirme çalışmalarında önemi (The importance of wavelet spectra in structural health assessment studies), 3. International Conference on Earthquake Engineering and Seismology, İzmir, Türkiye, 2015.

[31] Sak ÖF, Beyen K. Hasar tanılamasında istatistiki değerlendirme yöntemlerinin zaman-frekans ortamında irdelenmesi (Study on statistical evaluation in time-frequency domain for damage identification). 5. International Conference on Earthquake Engineering and Seismology, Ankara, Türkiye, 2019.

[32] Beyen K. Damage identification analyses of a historic masonry structure in T-F domain. Teknik Dergi 2021; 32(2): 10577-10610.

ESKİŞEHİR TECHNICAL UNIVERSITY JOURNAL OF SCIENCE AND TECHNOLOGY
A- APPLIED SCIENCES AND ENGINEERING

2022, 23(3), pp. 207-215, DOI: 10.18038/estubtda.1038059

RESEARCH ARTICLE

EFFECT OF HYDROTHERMAL CARBONS CONTENT ON WEAR PROPERTIES OF POLYETHYLENE MATRIX COMPOSITES

Yasin AKGUL *

Metallurgical and Materials Science Engineering Department, Karabuk University, Karabuk, Turkey

ABSTRACT

Compared to commonly used carbonaceous materials such as carbon nanotubes or graphene nanoplatelets, hydrothermal carbons (HTCs) are obtained with environmentally friendly approaches at a lower cost. Although HTCs have a wide application area such as batteries, magnetic materials, supercapacitors, adsorbent materials, etc., there are few studies on the usage of HTC as reinforcement material for composites. In this study, polyethylene matrix composites containing different amounts (0.5 wt.%, 1 wt.%, 2 wt.%) of HTCs were fabricated via the injection molding process. The effect of HTCs content on the wear properties of polyethylene matrix composites was investigated. Reciprocating wear tests were performed by applying different loads at dry sliding conditions. To correlate with wear results, the mechanical properties of samples were determined by tensile and impact tests. Also, FTIR and DTA analyzes were conducted to understand the effect of HTCs on the structural and thermal properties of composites. Results show that the addition of HTCs led to the enhancement of mechanical and tribological properties of polyethylene at lower amount reinforcement ratios. Thus, it can be said that HTCs could be an alternative carbonaceous reinforcement material for polymer matrix composites.

Keywords: Hydrothermal carbons, Polyethylene, Wear properties, Composite materials, Mechanical properties

1. INTRODUCTION

Polyethylene (PE) is one of the most used polymers for tribological applications such as biomedical and military because of its high wear resistance [1]. However, the tribological properties of PE don't completely satisfy the requirements in these fields [2]. Therefore, the wear properties of PE need to be improved. For this purpose, many studies have been conducted to enhance wear resistance of PE with the addition of different types of reinforcements [3].

In recent years, carbonaceous reinforcements such as graphene nanoplatelets (GNPs) and carbon nanotubes (CNTs) have become popular for polymer matrix composites due to their superior mechanical properties. GNPs have a high elastic modulus (~1 TPa) while CNTs have nearly 0.27 TPa to 1.47 TPa of elastic modulus [4]. In addition to mechanical properties, these fillers act as a solid lubricant which causes a lower coefficient of friction compared to ceramic and metal fillers [5].

Johnson et al. [6] reported tribological properties of CNTs /PE composites. It was shown that the wear rates of the composites decreased with increasing CNTs content (1%, 3%, and 5%). Composites containing 5% wt. CNT presented a 50% better wear resistance compared to pure PE. In another study, Fouad and Elleithy [7] produced PE matrix composites containing GNPs at different weight ratios (2%, 4%, and 8%). It was observed that the hardness and wear resistance of pure HDPE were enhanced with the addition of GNPs up to 4 wt.%. However, when the GNP ratio increased to 8%, although the hardness value increased, the wear resistance decreased due to poor matrix-reinforcement bonding. McNally et al. [8] melt blended PE with 0.1, 0.5, 1, 3, 5, 7, 8.5 and 10 wt.% MWCNTs. It was reported that the yield strength of composites was improved up to 7 wt.% CNTs addition. In another similar study, Bourque et al. [9] reinforced PE with GNPs (0.1 wt.% to 15 wt.%) via twin-

*Corresponding Author: yasinakgul@karabuk.edu.tr
Received: 17.12.2021 Published: 27.09.2022

screw extrusion. Results show that the yield strength of samples enhanced with the increase in the GNPs ratio.

As mentioned above, GNPs and CNTs had a positive effect on the mechanical and wear properties of polyethylene matrix composites. However, they have been produced with high production costs [10]. Also, in their production, environmentally harmful chemicals are used [11]. Hydrothermal carbons (HTCs) can overcome the disadvantages of these carbonaceous reinforcements. HTCs are produced from eco-friendly biomass such as pure carbohydrates, lignocellulose, simple sugars sea plant derivate, food wastes, etc. without using harmful chemicals at low operating temperatures [12]–[14]. HTCs have a wide application area such as batteries [15], magnetic materials [16], supercapacitors [17], adsorbent materials [18], etc.

Previous studies show that using HTCs as a reinforcement material led to the enhancement of tribological and mechanical properties of metal matrix composites [10], [11]. However, to the best of my knowledge, there is no study on the effect of HTCs on the wear properties of polymer matrix composites. In this study, the effect of HTCs content on the wear properties of polyethylene matrix composites was investigated. Also, structural, thermal, and mechanical properties of PE/HTCs composites were studied.

2. EXPERIMENTAL METHODS

2.1. Materials

PE powders with trade code LUMICENE® M3427 were supplied from Total Polymers (Belgium). The melting point of PE powders is 123 ℃ and their melt flow index is 3.1. To synthesize HTCs, 1 gr of glucose (Merck) was dissolved in 15 ml distilled water. Then, obtained suspension was poured into stainless steel autoclave. The autoclave was put into a furnace at 210 ℃ for 24 hours of residence time. After the cooling, solid carbon products were separated by filter paper and dried in a furnace at 105 ℃ for 1 hour. SEM images of the produced HTCs was shown in Figure 1.

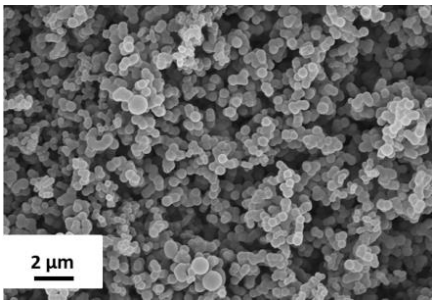

Figure 1. SEM images of produced HTCs.

2.2. Production of Samples

The production diagram of PE-HTCs composites was presented in Figure 2. The produced HTCs and PE powders were mixed in the 3D mixer (Turbula®) for 2 hours. Then, mixed powders were fed to an injection molding device. The temperature profile of the injection molding device was set at 235℃, 245℃, 265℃ from hopper to die. Dog-bone shaped samples were produced.

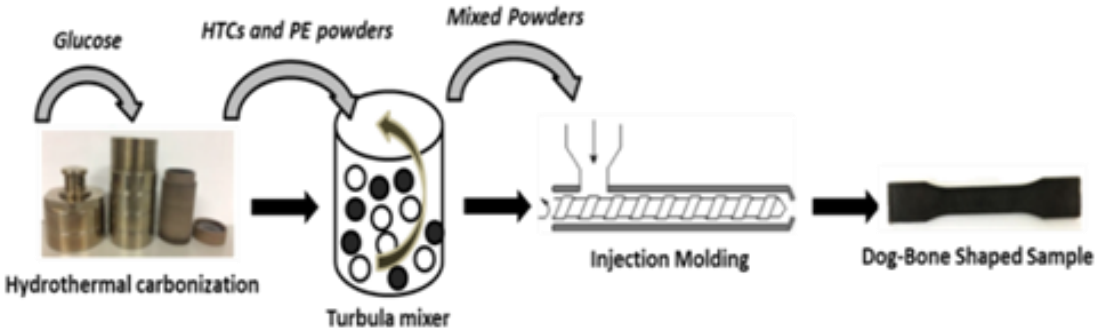

Figure 2. Production diagram of PE-HTCs composites

2.3. Characterization

Fourier Transform Infrared Spectroscopy (FTIR) spectrums of samples were obtained using the Bruker Alpha FTIR device. The resolution was set to 24 cm^{-1} and twenty-four scans were recorded for each sample in the range of 600–4000 cm−1. The thermal properties of the samples were investigated via Hitachi STA 7300 Differential Thermal Analysis (DTA) device. The samples were heated up to up to 200 °C with a heating rate of 10 °C/min. The analysis was conducted under nitrogen gas and the gas flow rate was 2 ml/min. The % crystallinity (Xc) of samples was calculated according to the following equation (1):

$$X_c = (\Delta H_m)/\Delta H°_m) \text{ x } 100\% \quad (1)$$

where ΔH_m is the melting enthalpy after thermal history, $\Delta H°_m$ is the enthalpy of 100% crystallization of HDPE [19]. The tensile test was performed with a Shimadzu tensile testing machine at room temperature at 5 mm/min test speed. For the impact test, the samples were cut in a dimension of 70 × 12.7 × 3.2 mm, and the test was applied to unfnotched samples using a Zwick/Roell RKP 450 device. The wear test was applied by using the UTS Tribometer device for samples under three different loads (20, 30, and 40 N), for 100 m sliding distance, using AISI 52100 steel ball, at 10 mm stroke distance. A schematic drawing of the wear test device was presented in Figure 3.

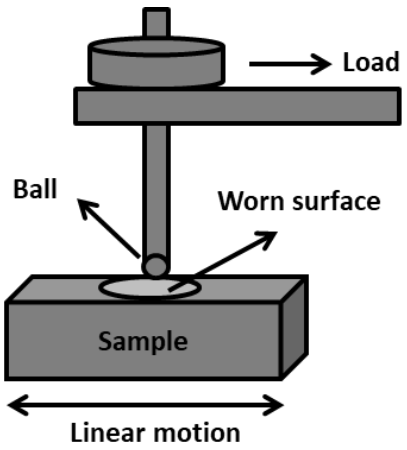

Figure 3. Schematic representation of the wear test device.

Wear rates of samples were determined using the volume loss method and calculated using equation (2).

$$\text{Wear rate } (W_r) = W_v/l \quad (2)$$

Where W_v is worn volume and l is the sliding distance. The worn surface area was measured with the Mitutoyo SJ-410 instrument. W_v was calculated by multiplying worn surface and stroke distance [20]. Zeiss Ultra Plus Scanning Electron Microscope was used for examination of the HTCs and worn surfaces of samples after gold coating.

3. RESULTS AND DISCUSSION

3.1. Structural and Thermal Properties

Figure 4 illustrates the FTIR spectra of samples. Samples have two peaks at nearly 2920 and 2852 cm^{-1}. These peaks can be attributed to C–H asymmetric and C–H symmetric stretching vibrations in -CH_2-, respectively. Also, there are smaller peaks at nearly 1466 cm^{-1} and 723 cm^{-1} due to C–H deformation vibrations in –(CH_2)n– and C–C rocking vibrations in –(CH_2)n–, respectively [21]. There is no new peak formation with the addition of HTCs to the PE matrix. Therefore, it can be said that there is no chemical interaction and HTCs were mechanically attached to the PE matrix.

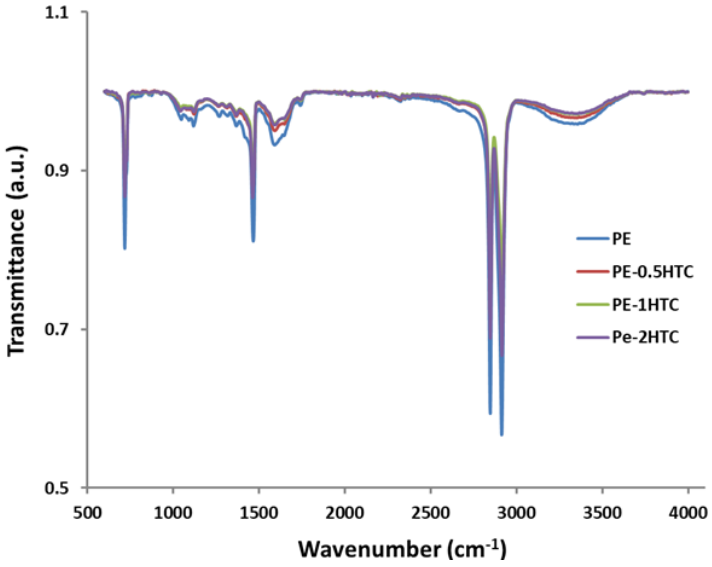

Figure 4. FTIR spectra of samples.

The melting temperatures and crystallinity of all samples were seen in Table 1. It can be said that melting points of composites were not changed with increasing HTCs content, significantly. The melting points of composites range from 119.2 ℃ to 119.5 ℃, while pure polyethylene is 118.2 ℃. This result was in good agreement with the findings of Thongruang et al [22].

On the other hand, HTCs reinforced composites have lower crystallinity than pure polyethylene. This can be attributed to the friction between HTCs and polymer chains may hinder the mobility of the macromolecular chain because hindering the mobility of the chains can obstruct formation of highly ordered alignment of the crystal lattice [23]. Also, it is worth the note that the crystallinity of composites was decreased with increasing HTCs content. PE-2HTC showed the lowest crystallinity and its crystallinity was %8 lower compared to PE.

Table 1. Melting temperature and crystallinity of samples

Sample	Melting Temperature (℃)	Crystallinity (%)
PE	118.2	75
PE-0.5 HTC	119.2	72
PE-1 HTC	119.3	70
PE-2 HTC	119.5	69

3.2. Mechanical Properties

Absorbed energies during the impact test and tensile strength of samples were shown in Figure 5. Addition of HTCs up to 1 wt.% reinforcement ratio improved the mechanical properties of pure PE. The tensile strength and absorbed energy amounts of PE increased from 12.4 MPa to 14.6 MPa and from 6.5 J to 8.5 J with the addition of 1 wt.% HTCs, respectively. As mentioned above, HTCs were only mechanically attached to the PE matrix. When force is applied during the tensile test, the polymer chains start to move, it can be estimated that HTC provides an increase in tensile strength by mechanically preventing polymer chain movement [5]. Also, it may be noted that HTCs can block crack propagation during the applied impact load.

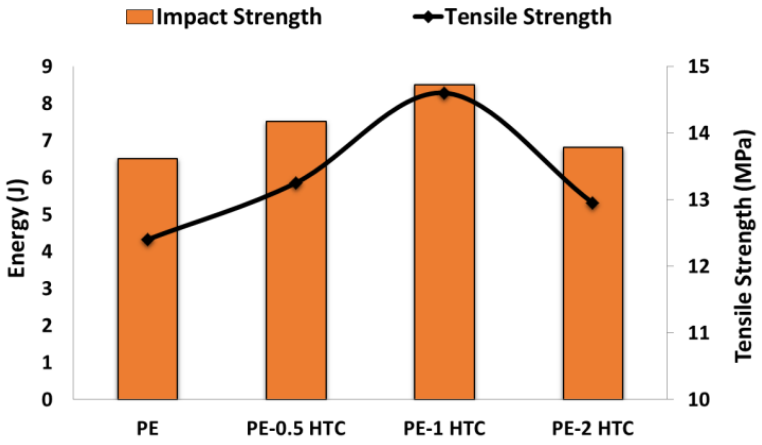

Figure 5. Absorbed energies and tensile strength of samples.

However, when the HTC ratio increased from 1 wt.% to 2 wt.%, there was a decrease in both tensile strength and impact strength. It is well known that solid micro-nano-particle reinforcements tend to agglomerate in polymer matrix. Therefore, it was thought that HTCs agglomerated in the matrix for PE-2HTC sample which have more HTC content compared to the others and this agglomeration caused a weaker matrix-reinforcement interface. Poor matrix-reinforcement interface can cause a decrease in mechanical properties.

3.3. Wear Properties

The wear properties of composites play an important role in the application of these materials in engineering applications [24]. The wear rates of produced samples under three applied loads (20, 30, and 40 N) were presented in Figure 6. It was observed that the wear rates of samples were increased with the increment of the applied load. This may be explained with that repeated higher loads on the surfaces of samples cause higher friction force [25].

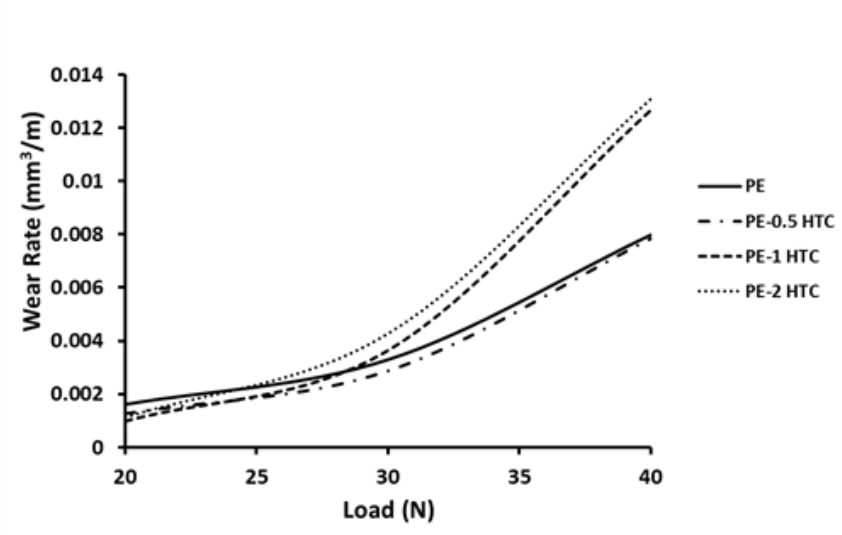

Figure 6. Wear rates of samples

Up to 20 N applied load, the addition of HTCs led to the enhancement of wear resistance of pure PE. Wear rates of PE, PE-0.5HTC, PE-1HTC and PE-2HTC were $1.61*10^{-3}$ mm^3/m, $1.26*10^{-3}$ mm^3/m, $0.98*10^{-3}$ mm^3/m and $1.12*10^{-3}$ mm^3/m, respectively. PE-1HTC had the lowest wear rate at this load. According to Archard's wear law, harder materials exhibit a lower wear rate [26]. Thus, it may be argued that the results were coherent with the mechanical properties of samples. Also, Yetgin and Colak observed similar findings in graphite filled polypropylene composites [27].

However, the wear rates of PE-1HTC and PE-2HTC were higher than PE under 40 N applied load. When the applied load was increased from 20 N to 40N, wear resistance of the PE-1HTC and PE-2HTC decreased 58 % and 64 % respectively. This can be attributed to poor interfacial bonding between HTCs and PE because much more wear debris can be occurred at higher applied loads during the wear test for samples which have agglomerated HTCs [5].

.

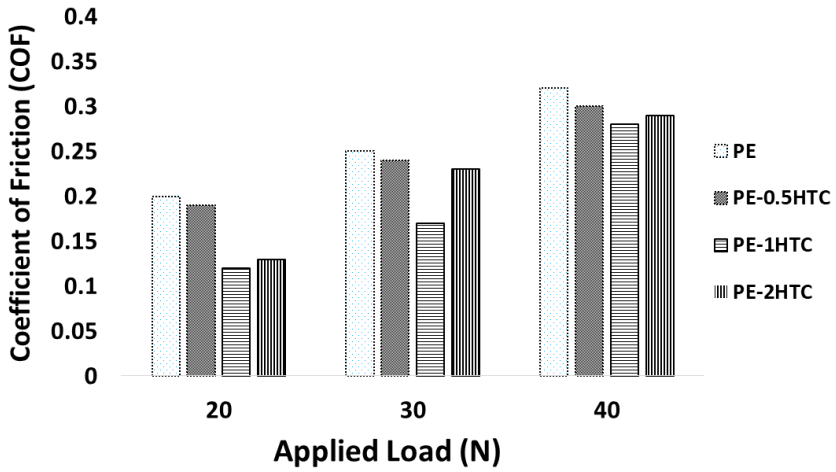

Figure 7. The coefficient of friction values of samples

Figure 7 presents the coefficient of friction (COF) values of samples. Carbonaceous reinforcements including HTCs have a lubricant effect [11] so the coefficient of friction values of samples were

decreased with the addition of HTCs. On the other hand, COF values were increased when the applied load increased due to non-uniform friction at higher reapplied loads.

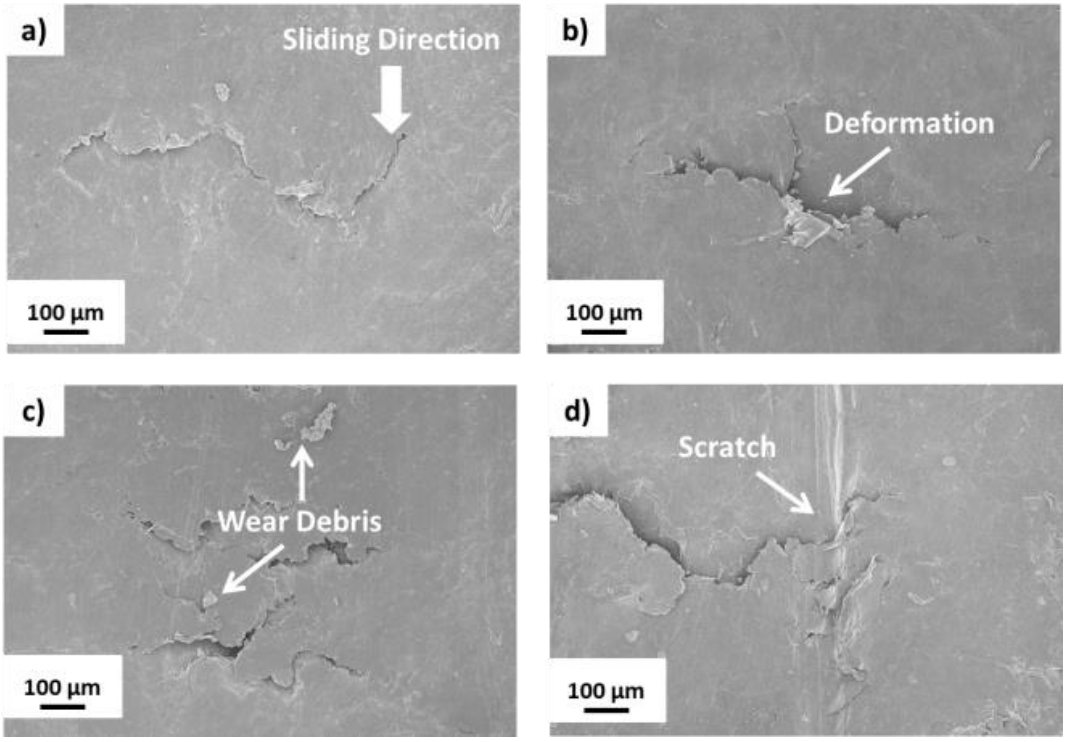

Figure 8. Worn surfaces of samples a) PE, b) PE-0.5HTC, c) PE-1HTC, d) PE-2HTC

Figure 8 shows the SEM images of the worn surfaces of samples. It was seen that wear debris occurred for both HTC reinforced composites and pure PE. This indicated the formation of an abrasive wear mechanism. Parallel to the sliding direction, scratches can be seen for PE-2HTC. This result also confirmed the formation of an abrasive wear mechanism.

4. CONCLUSIONS

In this study, PE/HTCs composites were produced via 3-D mixing and injection molding processes. The effect of HTCs on the tribological properties of polymer matrix composites was investigated for the first time. It was found that there is no chemical bonding between HTCs and PE matrix. The tensile and impact properties of pure PE were improved by nearly 18% and 31% with 1 wt.% HTCs addition, respectively. Wear test results showed the same trend as mechanical test results at lower applied loads and PE-1HTC showed 39% better wear properties than pure PE. Also, HTCs reinforced composites had lower COF values than pure PE due to the lubricant effect of HTCs. However, when an applied load was increased, PE-1HTC and PE-2HTC had lower wear resistance than PE due to the poor interfacial bonding between matrix and reinforcement. To sum up, the usage of HTCs as reinforcement material showed a positive effect on the wear properties of PE matrix composites. Therefore, it can be taught that HTCs may be promising reinforcement material for polymer matrix composites.

ACKNOWLEDGEMENTS

The author would like to thank the Karabuk Iron and Steel Institute for their support in conducting analyzes.

CONFLICT OF INTEREST

The author stated that there are no conflicts of interest regarding the publication of this article.

REFERENCES

[1] Liu T, Wood W, Li B, et al. Effect of reinforcement on wear debris of carbon nanofiber/high density polyethylene composites: Morphological study and quantitative analysis. Wear 2012; 294: 326–335.

[2] Goodman S, Lidgren L. Polyethylene wear in knee arthroplasty: a review. Acta Orthopaedica Scandinavica 1992; 63: 358–364.

[3] Liu T, Li B, Lively B, et al. Enhanced wear resistance of high-density polyethylene composites reinforced by organosilane-graphitic nanoplatelets. Wear 2014; 309: 43–51.

[4] Lee C, Wei X, Kysar JW, et al. Measurement of the Elastic Properties and Intrinsic Strength of Monolayer Graphene. Science 2008; 321: 385–388.

[5] Akgul Y, Ahlatci H, Turan ME, et al. Influence of carbon fiber content on bio-tribological performances of high-density polyethylene. Materials Research Express 2019; 6: 125307.

[6] Johnson BB, Santare MH, Novotny JE, et al. Wear behavior of carbon nanotube/high density polyethylene composites. Mechanics of Materials 2009; 41: 1108–1115.

[7] Fouad H, Elleithy R. High density polyethylene/graphite nano-composites for total hip joint replacements: Processing and in vitro characterization. Journal of the mechanical behavior of biomedical materials 2011; 4: 1376–1383.

[8] McNally T, Pötschke P, Halley P, et al. Polyethylene multiwalled carbon nanotube composites. Polymer 2005; 46: 8222–8232.

[9] Bourque AJ, Locker CR, Tsou AH, et al. Nucleation and mechanical enhancements in polyethylene-graphene nanoplate composites. Polymer 2016; 99: 263-272.

[10] Simsir H, Akgul Y, Erden MA. Hydrothermal carbon effect on iron matrix composites produced by powder metallurgy. Materials Chemistry and Physics 2020; 242: 122557.

[11] Arsun O, Akgul Y, Simsir H. Investigation of the properties of Al7075-HTC composites produced by powder metallurgy. Journal of Composite Materials 2021; 0021998321990877.

[12] Simsir H, Eltugral N, Karagoz S. Hydrothermal carbonization for the preparation of hydrochars from glucose, cellulose, chitin, chitosan and wood chips via low-temperature and their characterization. Bioresource technology 2017; 246: 82–87.

[13] Simsir H, Eltugral N, Karagoz S. Effects of acidic and alkaline metal triflates on the hydrothermal carbonization of glucose and cellulose. Energy & Fuels 2019; 33: 7473–7479.

[14] Simsir H, Eltugral N, Karagoz S. The role of capping agents in the fabrication of nano-silver-decorated hydrothermal carbons. Journal of Environmental Chemical Engineering 2019; 7: 103415.

[15] Simsir H, Eltugral N, Frohnhoven R, et al. Anode performance of hydrothermally grown carbon nanostructures and their molybdenum chalcogenides for Li-ion batteries. MRS Communications 2018; 8: 610–616.

[16] Siddiqui MTH, Nizamuddin S, Baloch HA, et al. Synthesis of magnetic carbon nanocomposites by hydrothermal carbonization and pyrolysis. Environmental Chemistry Letters 2018; 16: 821–844.

[17] Wei L, Sevilla M, Fuertes AB, et al. Hydrothermal carbonization of abundant renewable natural organic chemicals for high-performance supercapacitor electrodes. Advanced Energy Materials 2011; 1: 356–361.

[18] Sharma VT, Kamath SV, Mondal D, et al. Fe–Al based nanocomposite reinforced hydrothermal carbon: Efficient and robust absorbent for anionic dyes. Chemosphere 2020; 259: 127421.

[19] Polat S, Avcı A, Ekrem M. Fatigue behavior of composite to aluminum single lap joints reinforced with graphene doped nylon 66 nanofibers. Composite Structures 2018; 194: 624–632.

[20] Polat S, Sun Y, Çevik E, et al. Investigation of wear and corrosion behavior of graphene nanoplatelet-coated B4C reinforced Al–Si matrix semi-ceramic hybrid composites. Journal of Composite Materials 2019; 53: 3549–3565.

[21] De Geyter N, Morent R, Leys C. Surface characterization of plasma-modified polyethylene by contact angle experiments and ATR-FTIR spectroscopy. Surface and Interface Analysis: An International Journal devoted to the development and application of techniques for the analysis of surfaces, interfaces and thin films 2008; 40: 608–611.

[22] Thongruang W, Balik CM, Spontak RJ. Volume-exclusion effects in polyethylene blends filled with carbon black, graphite, or carbon fiber. Journal of Polymer Science Part B: Polymer Physics 2002; 40: 1013–1025.

[23] Hu C, Liao X, Qin Q-H, et al. The fabrication and characterization of high density polyethylene composites reinforced by carbon nanotube coated carbon fibers. Composites Part A: Applied Science and Manufacturing 2019; 121: 149–156.

[24] Akgul Y, Ahlatci H, Turan ME, et al. Mechanical, tribological, and biological properties of carbon fiber/hydroxyapatite reinforced hybrid composites. Polymer Composites 2020.

[25] Erden MA, Akgul Y, Kayabas O, et al. Mechanical Properties of Graphene-Nanoparticle and Carbon-Nanotube-Reinforced PE-Matrix Nanocomposites. Materiali in Tehnologije 2019; 53: 785–789.

[26] Turan ME, Sun Y, Akgul Y. Improved wear properties of magnesium matrix composite with the addition of fullerene using semi powder metallurgy. Fullerenes, Nanotubes and Carbon Nanostructures 2018; 26: 130–136.

[27] Yetgin S, Çolak M. Grafit katkılı polipropilen kompozitlerin mekanik ve tribolojik özelliklerinin incelenmesi. El-Cezeri Journal of Science and Engineering 2020; 7: 649–658.

ESKİŞEHİR TECHNICAL UNIVERSITY JOURNAL OF SCIENCE AND TECHNOLOGY
A- APPLIED SCIENCES AND ENGINEERING

2022, 23(3), pp. 216-222, DOI:10.18038/estubtda.1072801

RESEARCH ARTICLE

HIGH BRIGHTNESS 1908nm TM-DOPED FIBER LASER WITH POWER SCALING TO >75W

Salih Kağan KALYONCU *

Electro-Optics and Laser Systems Department, TÜBİTAK BİLGEM, Kocaeli, Turkey

ABSTRACT

In this paper, we have studied monolithic diode-pumped Tm-doped fiber laser to be used as a pump source for Ho-YAG systems. The cavity is designed to achieve high optical-to-optical efficiency and robustness against amplified spontaneous emission (ASE) induced parasitic oscillations via optimizing the doped fiber length and cavity parameters. Experimentally, we have demonstrated 1907.7 nm fiber laser with an output power of 79 W from 10/130 µm Tm-doped double clad fiber, enabling high brightness and radiance density as well. The laser cavity has a slope efficiency of ~55%, ASE suppression of > 40 dB and a near-diffraction-limited beam quality of M^2~1.07.

Keywords: Thulium doped fiber lasers, Mid-IR lasers, Parasitic oscillations

1. INTRODUCTION

Fiber lasers, compared to bulk crystal alternatives, offer unique compact, more reliable, robust, highly efficient, power scalable and high-brightness sources [1–4]. Thulium-doped fiber lasers (TDFL), having broad gain spectrum emitting at 1.8-2.1 µm regime facilitates many applications in emerging fields ranging from industry, remote sensing and medical to defense. In particular, 2 µm laser sources possessing lesser atmospheric scattering-distortion, and reduced thermal blooming compared to 1 µm alternatives facilitates long range LIDAR, free-space optical communication and directed energy systems [5]. Additionally, in material processing (cutting, welding, drilling) industry, while 1 µm lasers are frequently used in metal processing, 2 µm lasers with having significantly higher absorption peaks enables more efficient processing of non-metals such as plastics and glass materials [6]. Similarly, strong water absorption peaks around IR and mid-IR regime makes it possible to use 1.9-2.1 µm laser sources in medical applications especially in precise tissue surgery and lithotripsy [7-8]. On the other hand, high brightness Tm-doped fiber lasers (TDFL) around 1.9 µm constitutes an excellent pump source for solid-state laser systems (e.g. Ho-YAG) allowing for high quantum efficiency, are useful for in-band and core pumping of TDFLs and facilitates parametric frequency conversion to mid-IR and THz regime [9-11].

Thanks to the advances in commercially available semiconductor laser diodes (LD) emitting at ~790 nm, multi-clad fiber technology and high quantum efficiency due to cross-relaxation; a numerous amount of high power Tm-doped fiber lasers and amplifiers emitting ~2 µm have been successfully demonstrated [12]. In this approach, MOPA systems using large mode area (LMA) fibers with core diameter up to 25 µm are designed to achieve more than 1kW of output power at ~2.05 µm [13]. Yet, compared to multi-stage amplifier systems, high-power oscillators minimize cost and complexity providing more stability, robustness and precise control. Direct diode-pumped TDF oscillators operating below 2 µm have been reported at incremental power levels and different wavelengths as 170 W and 300W at 2050 nm [14-15], 278W at 1967 nm [16] and 185 W at 1950 nm [17].

*Corresponding Author: salih.kalyoncu@tubitak.gov.tr
Received: 13.02.2022 Published: 27.09.2022

To achieve emission at the far end of spectrum (> 2.05 μm), Ho-doped systems such as Tm-Ho co-doped fibers (more expensive and not fully established especially for high powers) and Ho: YAG (cost efficient and mature technology) are mostly favored. Hence, TDFLs emitting at 1908 nm plays a crucial role to pump such Ho: YAG systems. However, due to the severe gain competition (emission vs re-absorption) within the ASE spectrum which tends to lase at 1.95-1.98 μm, it is more challenging to design robust and stable TDFLs operating at 1908nm [18-19]. To develop such high power 1908 nm lasers, double-clad fibers (DCF) with core diameters > 15 μm are commonly used [18-22], which, however, degrades the beam quality, brightness $B \sim \left(\frac{Power}{(\lambda M^2)^2}\right)$, and radiance density $RD \sim \left(\frac{Intensity}{(\lambda M^2)^2}\right)$. Such single-mode fiber lasers with core diameters ≤ 10 μm and having high radiance density, on the other hand, facilitates power scalability by efficient beam combining, resonant in-band pumping of TDFLs and enhances gain medium excitation in solid-state lasers.

In this paper, we have demonstrated 1908 nm narrow linewidth single-mode fiber laser employing 10/130 μm Tm-doped fiber. As a design criteria, the doped fiber length and cavity parameters are optimized to achieve high output power and high ASE noise suppression for stable operation. Experimentally, we achieved 79 W near-diffraction-limited laser beam at 1907.7 nm with ~55% slope efficiency, > 40 dB ASE suppression and a M^2 of ~1.07.

2. EXPERIMENTAL SETUP

The proposed 1908 nm monolithic fiber laser is illustrated in Figure 1. The cavity is composed of a fused pump combiner (Nx1), a pair of fiber Bragg grating (FBGs) mirrors, Tm-doped DCF, cladding power stripper (CPS) and fiber pigtailed collimator. Laser diodes (LDs) emitting at 790nm [30W, 105/125 μm] are employed to couple ~150 W pump power into the cavity via using 7x1 multi-mode pump combiner with < 0.05 dB insertion loss. A pair of matched FBG mirrors, including high reflector (HR: λ_c=1908.07 nm, R=99.98%, and Δλ=2.81 nm) and output coupler (OC: λ_c=1908.03 nm, R=10.23%, and Δλ=1.08 nm) is used to form a resonating cavity. As the gain medium, 10/130 μm single-mode Tm-doped DCF with high clad absorption (α=8.37 dB/m at 789nm) and 0.15/0.46 numerical aperture (NA) is used. The doped-fiber length is optimized based on numerical analysis concerning the gain competition, namely the cavity is forced to lase at the wavelength with the lowest inversion (average excitation, n_2). To design such robust cavity against parasitic lasing with high ASE suppression, high conversion efficiency and adequate pump absorption, ~2 m TDF is employed as a gain medium. Even though it is less prominent for a-few-mode area fibers (≤10 μm), to attain a high beam quality (single-mode beam), namely to suppress higher order modes (HOMs) especially due to LP_{11} mode, and to achieve effective cooling, the gain fiber is wrapped spirally into a U-grooved channel (R_{min}= 75 mm) on a water-cooled Al heat sink.

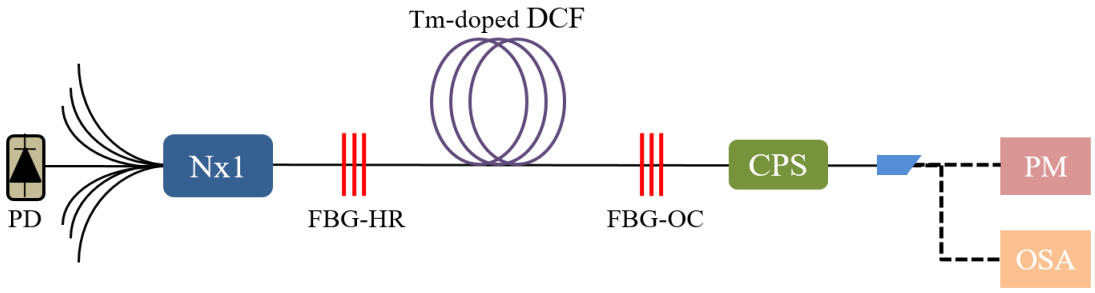

Figure 1. Experimental setup for 1908 nm monolithic CW fiber laser. PD: pump diode; PM: power meter; OSA: optical spectrum analyzer.

At the end of the cavity, a polymer-free CPS fabricated on a passive (Ge-doped) 10/130 µm DCF is used to strip unwanted cladding light stemmed from high NA residual pump light and low NA light escaped from core such as HOMs due to bending loss, lossy splices and ASE in gain medium. The coating of the DCF is window stripped and cladding surface is chemically etched (L=50 mm, ET=20 min) to create roughness on the glass clad. The performance of the etched fiber is tested in terms of the power handling capability, the stripping efficiency (Eff_{strip}), and the thermal load at the hot spot. Fabricated CPS packed in an Aluminum heat sink for mechanical protection and beam dump, can handle up to 100 W cladding power with ~17 dB attenuation and ~0.08 (°C/W) low thermal slope (TS), Figure 2.

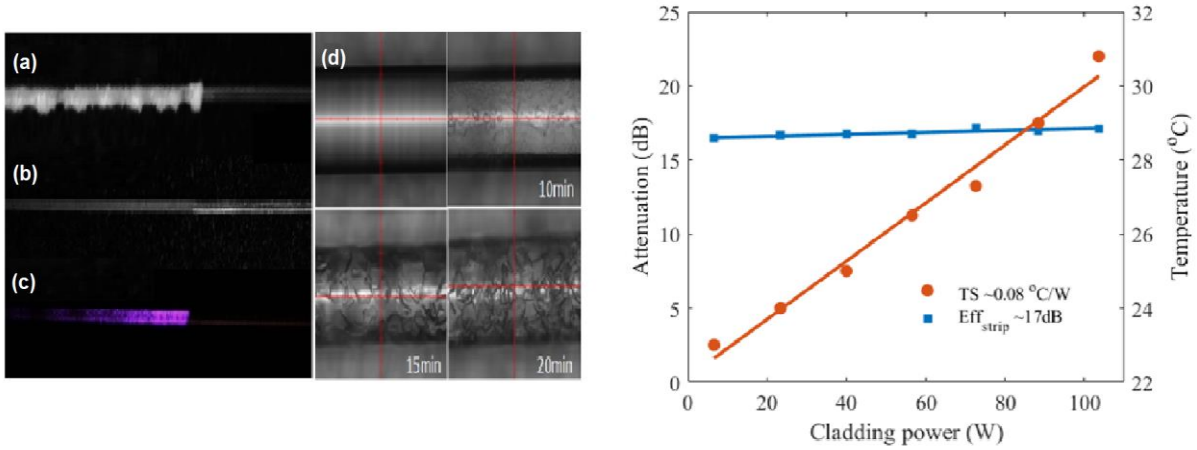

Figure 2. 10/130µm DCF after coating strip and etching process (a). The etched fiber (b) is examined under the white light (c). Microscope images (214µm x 265µm) of unetched and etched (for 10, 15 and 20mins) 10/130µm DCF for characterization (d). The stripping performance of fabricated CPS is studied in terms of stripping efficiency (Eff_{strip}) and thermal slope (TS) (e).

To test the laser performance, fiber coupled collimator with internal isolator (6.5 mm, <1 mrad divergence, >50 dB return loss) is spliced to the end of CPS to prevent any back reflections and hence the parasitic lasing. The power ratings, such as the output power and the slope efficiency, of the 1908 nm contınuous-wave (CW) fiber laser is measured with an air-cooled thermopile (Thorlabs S322C, 200 W) as illustrated in Figure 3. Thanks to the cross-relaxation in Thulium, the cavity produces up to 79 W single-mode laser beam with high slope efficiency of ~55%. As the performance of laser diodes strongly depends on the temperature, the emission shifts to the longer wavelengths (~1 nm/A) and gets locked to 790-793 nm (> 95% power in band) only at higher currents. At low currents, however, the pump light cannot be absorbed adequately due to the narrow absorption peak of the Tm at 790 nm and this, in turn, results in a reduction of the lasing efficiency and increase in thermal load on the CPS. Thus, unlike those driven in series, the pump diodes (x7) are operated one by one, making the slope efficiency stay almost constant as the pump power increases.

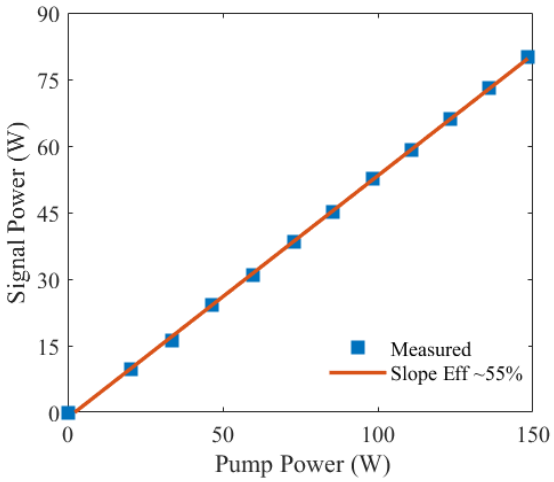

Figure 3. The output signal power versus pump power ratings. The cavity produces up to 79 W output power with approximately 55% slope efficiency.

The spectral content of the laser is simultaneously monitored by optical spectrum analyzer (OSA, Thorlabs 205C, 1.0-5.6 μm) to observe any ASE induced parasitic lasing. ASE mainly builds up in the spectral range of 1940–2000 nm and the parasitic oscillations in the vicinity of 1980 nm (peak emission for unforced cavity) is triggered as the signal power increases due to the high inversion. As shown in Figure 4, the laser emits at 1907.7 nm with a 0.13 nm spectral bandwidth and > 40 dB ASE noise suppression at full power of 79 W.

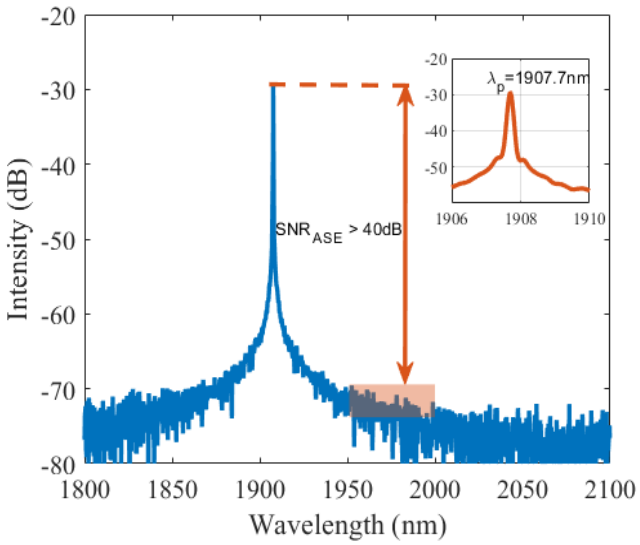

Figure 4. The spectral content of the laser cavity. The cavity lases at 1907.7nm with >40 dB ASE suppression within 1.95-2.0 μm spectral window.

Meanwhile, the beam quality, namely the spatial mode content, of the laser beam is characterized, and the M^2 factor is directly quantified by Ophir beam monitor (NanoModeScan) based on the second-moment method (99% at 4-sigma), as shown in Figure 5. The laser produces a near-diffraction-limited beam with ~120 mrad half-angle divergence and M^2 factor of 1.07 (M^2_x=1.06 and M^2_y =1.09), which indicates single-mode laser, in which the HOMs are suppressed, with high brightness and radiance density (scales quadratically with NA and core diameter). Such lasers with small beam-parameter

product (BPP) and high radiance density enables power scalability by efficient beam combining and enhances the gain medium excitation in solid-state lasers (i.e. Ho: YAG) with high overlap factor.

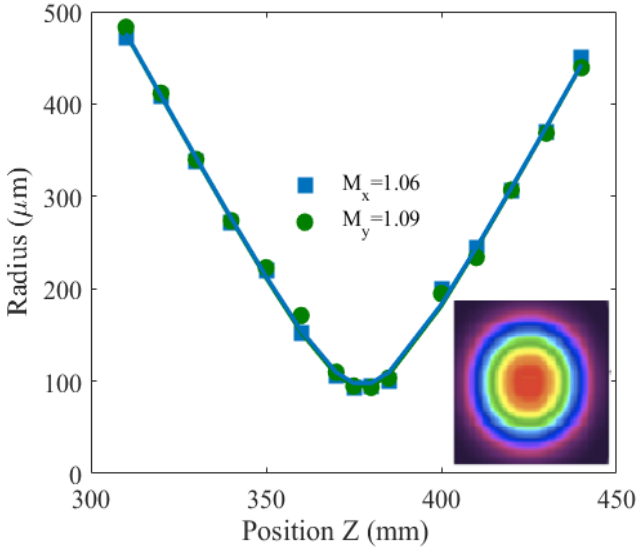

Figure 5. The far-field beam profile of the output laser at 79 W full-power. A diffraction-limited beam with M^2~1.07 is achieved. Beam profile at the waist (inset).

3. CONCLUSION

In conclusion, 1908 nm high brightness single-mode fiber laser employing10/130 μm double-clad Tm-doped fiber is demonstrated. The cavity parameters and doped-fiber length are optimized to achieve high robustness against parasitic lasing, high optical efficiency and adequate pump absorption. Experimentally, we have achieved 79 W output power with ~55% slope efficiency, peak emission at 1907.7 nm with > 40 dB ASE noise suppression and a diffraction-limited beam with an M^2 factor of 1.07. With the help of such a 1.9 μm high-brightness lasers, power scalability via efficient beam combining, in-band pumping of Ho-doped fiber laser/amplifier which reduces quantum defect and increases O-O efficiency, core-pumping in Ho-doped fiber laser/amplifiers and efficient excitation of gain medium in Ho-YAG solid-state lasers for medical and mid-IR frequency conversion application are facilitated.

CONFLICT OF INTEREST

The author stated that there are no conflicts of interest regarding the publication of this article.

REFERENCES

[1] DJ Richardson, Nilsson J, and Clarkson WA. High power fiber lasers: current status and future perspectives. J. Opt. Soc. Am. B 2010; 27 B63–B92.

[2] Limpert J, Roser F, Klingebiel S, Schreiber T, Wirth C, Peschel T, Eberhardt R and Tunnermann A. The rising power of fiber lasers and amplifiers. IEEE J. Sel. Top. Quantum Electron 2007; 13:537–545.

[3] Nilsson J, Ramachandran S, Shay TM and Shirakawa A. Introduction to issue of high power fiber lasers. IEEE J. Sel. Top. Quantum Electron 2009; 15: 1–2.

[4] Zając A, Dorosz D, Kochanowicz M, Skórczakowski M and Świderski J. Fiber lasers conditioning constructional and technological. Bull. Pol. Ac. Tech 2010; 58: 491–502.

[5] Russell J. De Young and Norman P. Barnes. Profiling atmospheric water vapor using a fiber laser LIDAR system. Appl. Opt 2010; 49: 562-567.

[6] Mingareev I, Weirauch, F, Olowinsky A, Shah L, Kadwani P and Richardson M. Welding of polymers using a 2 μm thulium fiber laser. Optics & Laser Technology 2012; 44: 2095–2099

[7] Kang HW, Lee H, Petersen J, Teichman J H and Welch A. J. Investigation of stone retropulsion as a function of Ho: YAG Laser pulse duration. Proc. SPIE 2006; 6078: Photonic Therapeutics and Diagnostics II 607815.

[8] Jansen ED, van Leeuwen TG, Motamedi M, Borst C, Welch AJ. Temperature dependence of the absorption coefficient of water for mid infrared laser radiation. Lasers in Surgery and Medicine 1994; 14: 258.

[9] Budni PA, Pomeranz LA, Lemons ML, Miller CA, Mosto JR and Chicklis EP. Efficient mid-infrared laser using 1.9-μm-pumped Ho: YAG and ZnGeP2 optical parametric oscillators. J. Opt. Soc. Am. B 2000; 17: 723-728.

[10] Kwiatkowski J, Jabczynski J K, Zendzian W, Swiderski J, Kaskow M and Gorajek L. A highly efficient resonantly pumped Ho: YAG laser. Proc. SPIE 2012; 8433: Laser Sources and Applications 84331J-1.

[11] Nicolas Dalloz, Thierry Robin, Benoît Cadier, Christelle Kieleck, Marc Eichhorn, and Anne Hildenbrand-Dhollande. High power Q-switched Tm3+, Ho3+- co-doped 2μm fiber laser and application for direct OPO pumping. Proc. SPIE 2019; 10897: Fiber Lasers XVI: Technology and Systems 108970J.

[12] Ramírez-Martínez NJ, Núñez-Velázquez M, Umnikov AA and Sahu JK. Highly efficient thulium-doped high-power laser fibers fabricated by MCVD. Opt. Express 2019; 27: 196-201.

[13] Ehrenreich T, Leveille R, Majid I and Tankala K. 1 kW, all-glass Tm: fiber lasers. SPIE Photonics West 2010; Fiber Lasers VII: Technology, Systems and Applications.

[14] Moulton P, Rines G, Slobodtchikov E, Wall K, Frith G, Samson B and Carter A. Tm-Doped Fiber Lasers: Fundamentals and Power Scaling. IEEE J. Sel. Top. Quantum Electron 2009; 15: 85.

[15] Samson B, Carter A, Tankala K, Majid I, Dong L and Hemming A. New fiber developments for amplifiers operating at 1μm and 2μm. SPIE Security + Defense 2013; 8898-29.

[16] Till Walbaum, Matthias Heinzberg, Andreas Liem, Thomas Schreiber, Ramona Eberhardt, Andreas Tunnermann. Optimization of a diode-pumped thulium fiber laser with a monolithic cavity towards 278W and 1967nm. ASSL 2015.

[17] Hemming A, Simmakov N, Davidson A, Stepanov D, Corena L, Hughes M, Carmodh N, Davies P, Haub J, Carter A. An Efficient, Monolithic, Single Mode Thulium Fiber Laser. Workshop on Sp. Opt. Fibers., OSA 2013; Paper T2.4.

[18] Zhou R L, Ju Y L, Zhao J, Yang C and Wang Y Z. A theoretical and experimental investigation of an in-band pumped gain-switched thulium-doped fiber laser. Chin. Phys. B 2013; 22: 064208.

[19] Frith G, Carter A, Samson B, Farroni J, Farley K and Tankala K. Highly efficient 70W all-fiber Tm-doped laser system operating at 1908nm. OECC/ACOFT 2008; pp: 1-2.

[20] Bennetts S, Hemming A, Davidson A and Lancaster DG. 110W 790nm pumped 1908nm thulium fiber laser. OECC/ACOFT 2008; pp: 1-2.

[21] Hu Zhen-Yue, Yan Ping, Xiao Qi-Rong, Liu Qiang, Gong Ma-Li. 227-W output all-fiberized Tm-doped fiber laser at 1908 nm. Chin. Phys. B 2014; 23: 104206.

[22] Benjamin R. Johnson, Creeden D, Limongelli J, Pretorius H, Blanchard J, and Setzler S.D. Comparison of high power large mode area and single mode 1908nm Tm-doped fiber lasers. Proc. SPIE, Fiber Lasers XIII: Technology, Systems, and Applications 2016; 9728-972810.

ESKİŞEHİR TECHNICAL UNIVERSITY JOURNAL OF SCIENCE AND TECHNOLOGY
A- APPLIED SCIENCES AND ENGINEERING

2022, 23(3), pp. 223-232, DOI:10.18038/estubtda.1149416

RESEARCH ARTICLE

CHARACTERIZATION OF ARTIFICIALLY GENERATED 2D MATERIALS USING CONVOLUTIONAL NEURAL NETWORKS

Cahit PERKGÖZ [1], Mehmet Zahit ANGİ [1]

[1] Department of Computer Engineering, Faculty of Engineering, Eskişehir Technical University, Eskişehir, Turkey

ABSTRACT

Two dimensional (2D) materials have attracted many researchers due to the high-performance of the devices produced by these materials. There are different methods to produce 2D materials such as wet chemical synthesis, chemical vapor deposition (CVD), molecular beam epitaxy, atomic layer deposition, pulsed laser deposition (PLD), all of which require hours during the processes. Once the 2D structures are obtained, their properties including their defects should be revealed by different characterization tools. Characterization process also requires time and expertise. In this respect, deep learning methods such as Convolutional Neural Networks (CNN) can be a solution for the practical and rapid classification of the produced samples. However, there is not enough number of samples in most of the research laboratories because of the above-mentioned long experimental processes. This work presents the performance of a CNN algorithm using artificially created images of MoS_2, a commonly studied 2D semiconductor with a high potential in different electronics applications. The synthetic optical microscopic images including normal and defected MoS_2 flakes are generated by the intensities of light incident on different materials using Fresnel Equations. A deep CNN algorithm is constructed to detect the normal and defective samples. As a result of the experiments, an average of 88.9% accuracy was obtained. These results can be interpreted that CNN can be used in the future for the characterization of two-dimensional materials with a sufficient number of real images.

Keywords: MoS_2, Two-dimensional Materials, Fresnel Equations, Characterization, Deep Learning

1. INTRODUCTION

The scaling-down in transistors has led to great progress in silicon-CMOS technology. Reducing the physical dimensions at the beginning of the technology development resulted in an improvement in speed performance where the power density did not change much. However, in recent years, voltage scaling had to be carefully considered, given that lowering the threshold voltage makes it difficult to drive enough current, which means an increase in leakage current [1]. Remembering that there is the fundamental limit of subthreshold swing (SS), which has to be larger than 60 mV per decade at 300 K in conventional MOSFETs [2], the power density power in high-performance microprocessors is demanding complicated power management methods although reduction of physical dimensions has still been carried out up to present [3]. The problems related to the rise of static power and the leakage of current between the source and drain electrodes are examined under the concept of short-channel effects. In this sense, novel and smart strategies have to be pursued to overcome the aforementioned limitations and continue to improve the performance of transistors.

At this point, FETs that are made up of a 2 dimensional (2D) material based channel do not suffer from leakage current since the electrons are confined in atomically thin layers where the gate voltage provides a uniform operation [4]. Hence, lately, the potential of layered materials, namely 2D materials, have been recognized for advanced technological applications [5]. Such 2D materials present unusual properties that do not exist unconventional bulk materials. The most widely studied 2D material is

*Corresponding Author: cahitperkgoz@eskisehir.edu.tr
Received: 27.07.2022 Published: 27.09.2022

graphene [6], which is a sheet of carbon atoms atomically thin where its pristine form has a zero-bandgap and is counted as a semimetal. However, the lack of an energy bandgap makes graphene unsuitable for FET applications, despite different efforts to open a bandgap. Therefore, other 2D materials have started to come into play, mainly semiconductor transition metal dichalcogenides (TMDs) as they possess a bandgaps in the visible and infrared spectral range. On the other hand, there are still critical challenges related to production and characterization of these 2D materials to be utilized as a compelling technology.

Chronologically, first 2D materials were realized by using mechanical exfoliation, which were limited to some tens of micrometers [7]. Other methods such as wet chemical synthesis, chemical vapor deposition (CVD), molecular beam epitaxy, atomic layer deposition, pulsed laser deposition (PLD) have been studies to realize such 2D materials [8], where among these, the CVD process has advanced in years and it is recognized as a high potential technique that can provide scalable 2D materials [9, 10] and it is well-suited with microelectronic processes [11]. Nevertheless, the activation of gaseous reactions , controllability of the formed structures and wafer-size fabrication persist as critical issues [12]. In addition to these, 2D material characterization includes time-consuming and sometimes expensive routes such as Raman scattering spectroscopy, atomic force microscopy (AFM), photoluminescence (PL) spectroscopy, which are not suitable for large-area analysis [13, 14]. If the usage of an optical microscope is enhanced also as a tool to understand the uniformity and layer thickness then such a practical and low-cost option of characterization tool would make significant contribution to the field considering that mainly, an optical microscope is the first tool that is utilized to investigate the obtained 2D materials [15].

CVD grown 2D materials can include different number of layers, defects, gain boundaries, wrinkles and oxide formations, which can affect the device operation of a device of which the active region is made up of 2D materials. Hence, recently, there are ongoing researches that utilize a relatively simple characterization tool, optical microscope, to make detailed analyses of 2D materials while still keeping rapidness and large-area examination where these techniques engage deep learning-based methods is established on artificial neural networks [16-18].

There is an increasing usage of these artificial intelligence techniques in diverse fields including medicine, diagnosis, biology, physics, and electronics [19-22]. Image processing, classification, clarifying and creating images are also among the other applications [23]. Out of various deep learning methods, convolutional neural networks (CNN) out-performs other techniques for image identification and arrangement [24-26].

This article mainly focuses on obtaining a method to decide if CVD grown 2D TMD materials, namely MoS_2 monolayers, are suitable to be employed in devices such as transistors, sensors or detectors. Such formations will be referred as intact structures hereafter. In this study, a deep learning method for the characterization of 2D MoS_2 will be applied where artificial images, which mimic the images that are obtained by optical microscopy tool, are produced using Fresnel equations for training and testing.

2. METHODS

2.1. Fresnel Equations

Light, as an electromagnetic wave, incident on a surface is partially reflected and partially refracted. According to the Snell's law, the reflection and transmission angles of these waves can be calculated. Based on these angles, Fresnel equations, which define the ratio of the electric field of reflected and refracted waves, are derived [27, 28]. A bright-field microscope creates images by using the contrast of the reflected light from the different points of the sample surface. Therefore, generating synthetic images could be possible if the physical properties of both the substrates and the deposited materials are known.

The cross section of a sample for a typically grown 2D material to be examined under the optical microscope is given below.

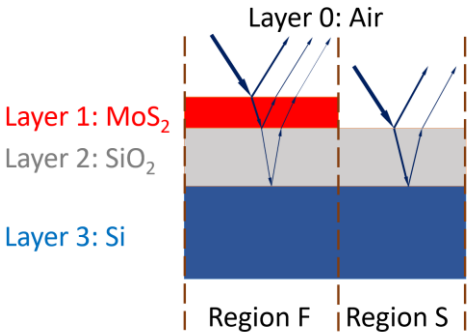

Figure 1. Cross-section of a grown 2D material (MoS_2).

The optical contrast of the sample for two regions can be defined as in Equation 1.

$$C = \frac{I_F - I_S}{I_F + I_S} \tag{1}$$

where I_F and I_S are the light intensities in region *F* and region *S*, respectively. As it is shown in Figure 1, region *F* has a 2D material (MoS_2) on the substrate (SiO_2/Si), whereas region *S* has only the substrate (SiO_2/Si). Therefore, light intensities reflected by two different regions would be different and can be defined as:

$$I_F = |\bar{r}_F r_F| \tag{2}$$
$$I_S = |\bar{r}_S r_S| \tag{3}$$

where, r_F and r_S are the reflection Fresnel coefficients for region *F* and *S*, respectively. These two values should be analyzed for two cases where in region *S* there is only the substrate (3 layers including air, SiO_2 and Si) and in region *F* the substrate is covered with the 2D material (4 layers including air, MoS_2, SiO_2 and Si). The related reflection Fresnel coefficients for the regions are defined as in Equation 4 and 5.

$$r_F = \frac{r_{01}e^{i(\emptyset_1+\emptyset_2)} + r_{12}e^{-i(\emptyset_1-\emptyset_2)} + r_{23}e^{-i(\emptyset_1+\emptyset_2)} + r_{01}r_{12}r_{23}e^{i(\emptyset_1-\emptyset_2)}}{e^{i(\emptyset_1+\emptyset_2)} + r_{01}r_{12}e^{-i(\emptyset_1-\emptyset_2)} + r_{01}r_{23}e^{-i(\emptyset_1+\emptyset_2)} + r_{12}r_{23}e^{i(\emptyset_1-\emptyset_2)}} \tag{4}$$

$$r_S = \frac{r_{01} - r_{12}e^{-i2\emptyset_1}}{1 + r_{01}r_{12}e^{-i2\emptyset_1}} \tag{5}$$

where, Fresnel coefficients (r_{ij}) are the functions of refractive indexes (n_i and n_j) of the overlapping layers *i* and *j*:

$$r_{ij} = \frac{(n_i - n_j)}{(n_i + n_j)} \tag{6}$$

and $\emptyset_i$ is the phase shift resulted by the propagation of the light in the medium of layer i. $\emptyset_i$ is expressed as:

$$\emptyset_i = \frac{2\pi n_i d_i}{\lambda} \tag{7}$$

where n_i, d_i and λ are the refractive index, the thickness of the medium i, and the wavelength of the light, respectively. The index i is 0 for air, 1 for MoS_2, 2 for SiO_2 and 3 for Si.

Hence, for an artificially created structure shown in Figure 1 with the specific values of the refractive indices of the media, the intensities of light for the two regions can be obtained under different wavelengths. Then, an artificial RGB image can be constructed for different thicknesses from which the 2D material can be characterized.

2.2. Convolutional Neural Networks

Hubel and Wiesel discovered "simple cells" and "complex cells" regarding the kitten visual cortex in 1959 [29]. According to this study, two kinds of cells are used for visual recognition. 20 years later, this study gave inspiration to Kunihiko Fukushima where the artificial neural network was designed to mimic such complex and simple cells [30]. The artificial cells were evidently not biological neurons, but rather mathematical operations. Fukushima's model was detecting simple shapes by simple cells whereas complex images (e.g., a human face) by complex cells which use lower-level complex cells or simple cells to get the features (e.g., an eye). In the 1990s, first modern convolution neural networks published by Yann LeCun [31]. In this research, LeCun created a convolutional neural network to recognize handwritten characters from the dataset which is called MNIST.

A CNN is a structure/concept that typically has three types of layers: convolution layer, pooling layer, and fully connected layer (Figure 2). The convolution layer and the pooling layer extract the features, and the fully connected layer is a typical neural network which maps the flattened layer vector to the output. Convolution layers perform convolution operation by some numbers of filters (kernels). Pixel values in digital images are processed by a kernel, a feature extractor. As you move through the layers, the extracted features also move from low-level to high-level patterns.

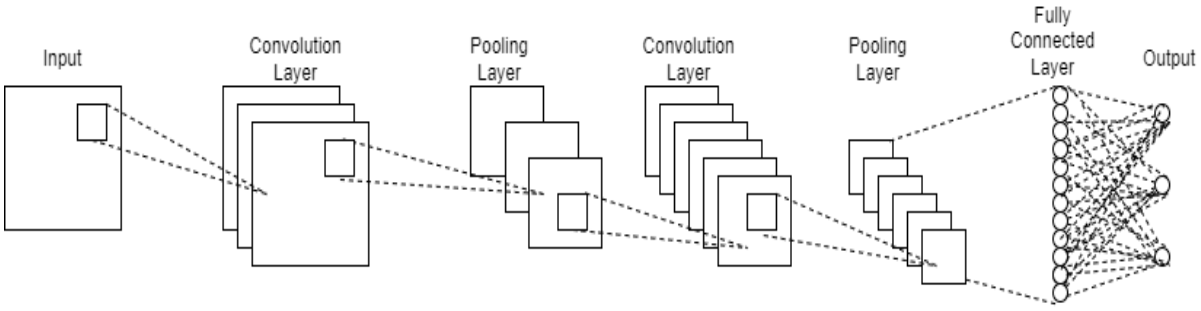

Figure 2. Convolutional Neural Network

Input Layer

The first layer of the CNN is the input layer from which the network receives the data raw data. The data size sent to this layer is critical for to the successful implementation of the model being intended. Choosing an image size rather large at the input increases high storage requirements as well as training and testing time per image. Furthermore, it can improve the network success rate. Choosing a smaller input image size can reduce memory requirements and reduce the training time. However, this time, smaller input image size will cause the depth of the network to decrease and the performance to deteriorate. Hence, for analyzing images, it is of importance to choose a proper image size in the input to reach the appropriate network depth, network success rate, and hardware computational cost.

Convolution Layer

The basis of the CNN is the convolution layer also recognized as the transformation level. This conversion process is built on looping specific filters throughout the full image. Therefore, a layered architecture comprises filters that are an integral part of the architecture with different filter sizes. Filters generate output data by means of employing a convolution operation to the preceding level image. Accordingly, this convolution operation provides the feature maps to be formed. The map of activation is the area where specific features are found for each filter. While training a CNN in the training set, each learning iteration changes the coefficients of these filters. In this way, the network can determine which areas of the data are essential for representation.

In case that we come up with some $M \times N$ size input (I) for any convolution operation and use an $m \times n$ filter "f" the size of the convolutional layer output X will become $(M-m+1) \times (N-n+1)$ and can be obtained by the following Equation.

$$X_{i,j} = \sum_{b=0}^{N-1} \sum_{a=0}^{M-1} W_{(i+a-1),(j+b-1)} f_{a,b} \tag{8}$$

Pooling Layer

The main objective of this layer is to decrease the input size for the next layer. The size of the depth is not changed by pooling operation. The process executed at this layer can be called "downsampling". The information loss due to the reduction size would provide two advantages. Firstly, it decreases the simulation time resulting from a smaller number of parameters in the network. Secondly, overfitting problem is avoided in deep learning. Although pooling operation is held by so called filters, this operates differently from the filters in convolution layer. For example, max pooling is that taking the maximum value of a group of pixels defined initially.

Fully Connected Layer

In a CNN architecture, after the successive convolution and pooling layers are completed, fully connected layers need to be considered. This layer takes inputs from the last pooling layer which are flattened. The number of hidden layers will vary in different architectures. Each neuron in each layer is fully connected to the previous and next layer neurons. Hence, this layer is called a fully connected layer. If the input of fully connected layer is represented by a vector h, layer number by l, neuron weights by a matrix W and bias vector by B, then the input of transfer function (σ) and the output of the layer will be defined as:

$$h^{in}{}_l = W_l \, h_{l-1}^{out} + B_l \tag{9}$$

$$y_l = \sigma(h^{in}{}_l) \tag{10}$$

Output Layer

This layer is the last layer of the fully connected layer. Classification happens at this level of this deep learning architecture. The output value of this layer is equal to the number of objects to be classified. Various transfer functions can be used in this layer.

3. RESULTS and DISCUSSIONS

The CNN algorithm developed for the classification of normal and defective stamps uses 10,000 artificial images of 100x100 pixels where 60% of the dataset is reserved for training, 20% for validation and 20% for testing. Half of the images contain normal flakes and the rest have distorted MoS_2 flakes. Distorted scales consist of two or more layers or have irregular structures. The images are created based on the intensity values for region *F* and *S* under red, green and blue light. For a normal flake, which has only one layer of MoS_2, $d_1 = 0.63$ nm [32]. The thickness of SiO_2 (d_2) is 300 nm [32]. The refractive indices n_i are given in Table 1 below for the colors in red, green, and blue [32].

Table 1. Refractive Indices

n	Red	Green	Blue
n_1(MoS_2)	4.3-1i	4.0-0.6i	4.5-1i
n_2 (SiO_2)	1.2	1.29	1.36
n_3 (Si)	3.84-0.016i	4.04-0.03i	4.67-0.14i

Based on the above parameters and Fresnel equations given in Section 2, the intact flakes are created and placed randomly on the images. For the case of defected flakes, non-uniform MoS_2 structures are created for various $d_1$values which will be multiples of one-layer MoS_2 thickness. Some examples for both of the cases are given in Figure 3.

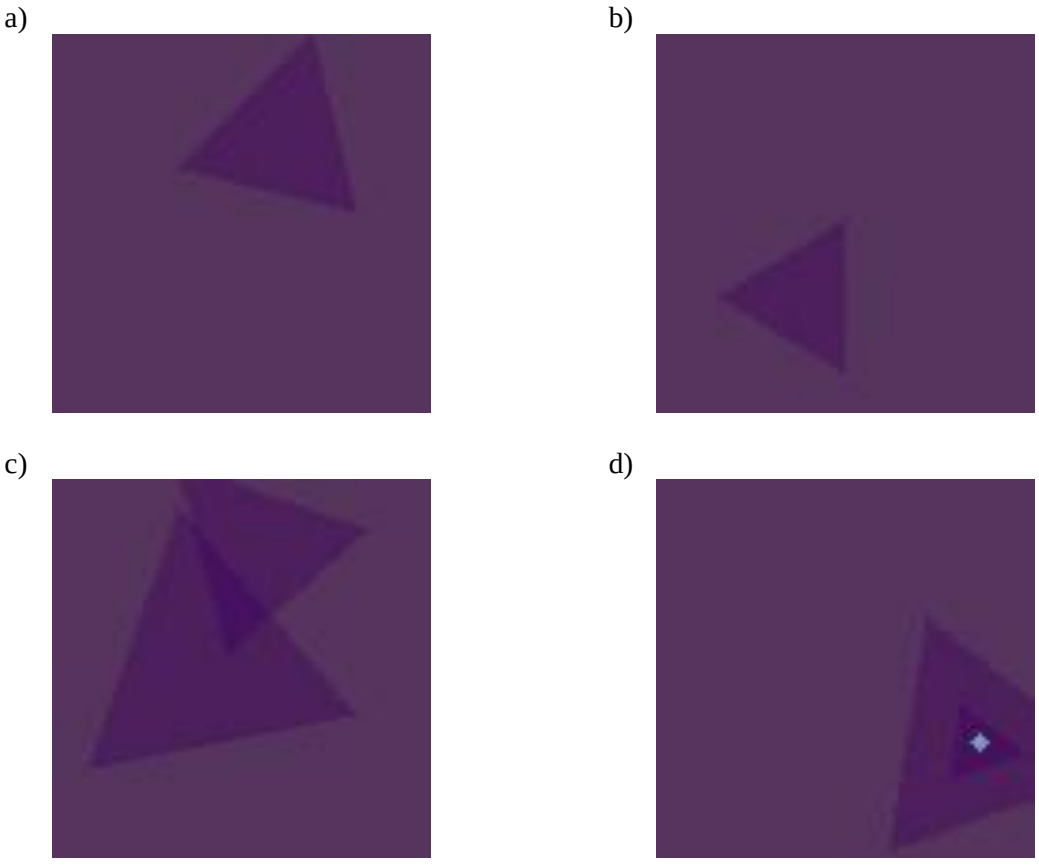

Figure 3. a, b) Intact flakes, c, d) defected flakes

In order to classify the uniformly and defected grown 2D materials, the CNN is structured as follows: There are 4 convolution layers where the convolution operation is held by 8, 16, 32 and 64 number of filters with 7x7, 7x7, 5x5 and 3x3 sizes, respectively. The pooling operation is held by choosing the

maximum of 2x2 pixels after each convolution layer. All the neurons in the network have LeakyRELU transfer function, except for the output neuron. A LeakyRELU transfer function is given in Figure 4.

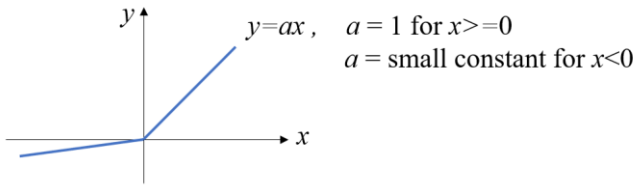

Figure 4. LeakyRELU Transfer Function

The output of the last maxpooling layer is flattened, which is the input vector of the fully connected layer of size 576. The fully connected layer has 64 neurons in the hidden layer and one output neuron with a sigmoid transfer function. The adaptive moment estimation (ADAM) optimizer is applied with a learning rate of 0.1.

The CNN algorithm is simulated 10 times with the same data set and the parameters on a PC computer which has a 3.5 GHz processor, of 128 GB RAM memory and RTX A5000 GPU. The created data has two classes of equal number of images. Performance metrics given in Equation 11-14 are used to find out the success of the CNN algorithm.

$$Accuracy = \frac{TP + TN}{TP + TN + FP + FN} \times 100 \tag{11}$$

$$Precision = \frac{TP}{TP + FP} \times 100 \tag{12}$$

$$Recall = \frac{TP}{TP + FN} \times 100 \tag{13}$$

$$F_1 Score = 2 \times \frac{Precision \times Recall}{Precision + Recall} \tag{14}$$

where, TP is the true positives, TN is the true negatives, FP is the false positives and FN is the false negatives.

The proposed method is simulated 10 times with the same parameters and the same data set. After obtaining the trained CNN structure, the test data is evaluated additionally. The performance metrics are obtained as given in Table 2 for the test data.

Table 2. Performance Metrics

Accuracy	Precision	Recall	F_1 Score
88.9%	89.8%	88.1%	88.9%

4. CONCLUSIONS

The production and characterization of nanomaterials is a time-consuming and demanding process, which required an expert to analyze and interpret the results. However, a CNN based deep learning method can do this laborious task in a very short time if it can be trained with a sufficient number of samples. In this work, first of all, 2D materials are created by using Fresnel equations and the material-specific values to obtain enough amount of data. The images of the flakes are constructed artificially assuming that a MoS_2 flake is on a SiO_2 layer which lays on a Si substrate. The intensity values of a normal light are calculated for both the regions with and without MoS_2 layer. From the intensity values the images are obtained for two classes of samples, based on the most encountered sample images. Then, a CNN structure is proposed to determine whether the sample is intact or defected. The classification performance of a CNN is evaluated by using these artificially created microscopic images that include two dimensional materials. Even though the images were artificially created, the high accuracy of the results have proved that CNN algorithms can also be used in the future with sufficient number of experimentally obtained data. Also, this work can be carried out for different types of 2D materials for the classification of intact and defected samples.

ACKNOWLEDGEMENTS

This work was supported by Eskişehir Technical University Scientific Research Projects Commission under the grant no: 22ADP144.

CONFLICT OF INTEREST

The authors stated that there are no conflicts of interest regarding the publication of this article.

REFERENCES

[1] Chang L, Frank DJ, Montoye RK, Koester SJ, Ji BL, Coteus PW, et al. Practical strategies for power-efficient computing technologies. Proceedings of the IEEE. 2010;98:215-36.

[2] Park JH, Jang GS, Kim HY, Seok KH, Chae HJ, Lee SK, et al. Sub-kT/q subthreshold-slope using negative capacitance in low-temperature polycrystalline-silicon thin-film transistor. Scientific reports. 2016;6:1-9.

[3] Attia KM, El-Hosseini MA, Ali HA. Dynamic power management techniques in multi-core architectures: A survey study. Ain Shams Engineering Journal. 2017;8:445-56.

[4] Chhowalla M, Jena D, Zhang H. Two-dimensional semiconductors for transistors. Nature Reviews Materials. 2016;1:1-15.

[5] Kong W, Kum H, Bae S-H, Shim J, Kim H, Kong L, et al. Path towards graphene commercialization from lab to market. Nature nanotechnology. 2019;14:927-38.

[6] Novoselov KS, Geim AK, Morozov SV, Jiang D-e, Zhang Y, Dubonos SV, et al. Electric field effect in atomically thin carbon films. science. 2004;306:666-9.

[7] Yi M, Shen Z. A review on mechanical exfoliation for the scalable production of graphene. Journal of Materials Chemistry A. 2015;3:11700-15.

[8] Bonaccorso F, Lombardo A, Hasan T, Sun Z, Colombo L, Ferrari AC. Production and processing of graphene and 2d crystals. Materials Today. 2012;15:564-89.

[9] Zhang Y, Yao Y, Sendeku MG, Yin L, Zhan X, Wang F, et al. Recent progress in CVD growth of 2D transition metal dichalcogenides and related heterostructures. Advanced materials. 2019;31:1901694.

[10] Aras FG, Yilmaz A, Tasdelen HG, Ozden A, Ay F, Perkgoz NK, et al. A review on recent advances of chemical vapor deposition technique for monolayer transition metal dichalcogenides (MX_2: Mo, W; S, Se, Te). Materials Science in Semiconductor Processing. 2022;148:106829.

[11] Liu D, Chen X, Yan Y, Zhang Z, Jin Z, Yi K, et al. Conformal hexagonal-boron nitride dielectric interface for tungsten diselenide devices with improved mobility and thermal dissipation. Nature communications. 2019;10:1188.

[12] Lin Z, McCreary A, Briggs N, Subramanian S, Zhang K, Sun Y, et al. 2D materials advances: from large scale synthesis and controlled heterostructures to improved characterization techniques, defects and applications. 2D Materials. 2016;3:042001.

[13] Özden A, Şar H, Yeltik A, Madenoğlu B, Sevik C, Ay F, et al. CVD grown 2D MoS_2 layers: A photoluminescence and fluorescence lifetime imaging study. physica status solidi (RRL)–Rapid Research Letters. 2016;10:792-6.

[14] Zhang J, Yu Y, Wang P, Luo C, Wu X, Sun Z, et al. Characterization of atomic defects on the photoluminescence in two‐dimensional materials using transmission electron microscope. InfoMat. 2019;1:85-97.

[15] Yorulmaz B, Özden A, Şar H, Ay F, Sevik C, Perkgöz NK. CVD growth of monolayer WS_2 through controlled seed formation and vapor density. Materials Science in Semiconductor Processing. 2019;93:158-63.

[16] Lin X, Si Z, Fu W, Yang J, Guo S, Cao Y, et al. Intelligent identification of two-dimensional nanostructures by machine-learning optical microscopy. Nano Research. 2018;11:6316-24.

[17] Saito Y, Shin K, Terayama K, Desai S, Onga M, Nakagawa Y, et al. Deep-learning-based quality filtering of mechanically exfoliated 2D crystals. npj Computational Materials. 2019;5:1-6.

[18] LeCun Y, Bengio Y, Hinton G. Deep learning. nature. 2015;521:436-44.

[19] Shinde PP, Shah S. A Review of Machine Learning and Deep Learning Applications. 2018 Fourth International Conference on Computing Communication Control and Automation (ICCUBEA)2018. p. 1-6.

[20] Shorten C, Khoshgoftaar TM, Furht B. Deep Learning applications for COVID-19. Journal of Big Data. 2021;8:1-54.

[21] Masubuchi S, Machida T. Classifying optical microscope images of exfoliated graphene flakes by data-driven machine learning. npj 2D Materials and Applications. 2019;3:1-7.

[22] Bharati S, Podder P, Mondal M. Artificial neural network based breast cancer screening: a comprehensive review. arXiv preprint arXiv:200601767. 2020.

[23] Masubuchi S, Watanabe E, Seo Y, Okazaki S, Sasagawa T, Watanabe K, et al. Deep-learning-based image segmentation integrated with optical microscopy for automatically searching for two-dimensional materials. npj 2D Materials and Applications. 2020;4:1-9.

[24] Yao G, Lei T, Zhong J. A review of convolutional-neural-network-based action recognition. Pattern Recognition Letters. 2019;118:14-22.

[25] Alzubaidi L, Zhang J, Humaidi AJ, Al-Dujaili A, Duan Y, Al-Shamma O, et al. Review of deep learning: Concepts, CNN architectures, challenges, applications, future directions. Journal of big Data. 2021;8:1-74.

[26] Bhuvaneswari V, Priyadharshini M, Deepa C, Balaji D, Rajeshkumar L, Ramesh M. Deep learning for material synthesis and manufacturing systems: a review. Materials Today: Proceedings. 2021;46:3263-9.

[27] Blake P, Hill E, Castro Neto A, Novoselov K, Jiang D, Yang R, et al. Making graphene visible. Applied physics letters. 2007;91:063124.

[28] Zhang W, Zhao Q, Puebla S, Wang T, Frisenda R, Castellanos-Gomez A. Optical microscopy–based thickness estimation in thin GaSe flakes. Materials Today Advances. 2021;10:100143.

[29] Hubel DH, Wiesel TN. Receptive fields of single neurones in the cat's striate cortex. The Journal of physiology. 1959;148:574.

[30] Fukushima K, Miyake S. Neocognitron: A self-organizing neural network model for a mechanism of visual pattern recognition. Competition and cooperation in neural nets: Springer; 1982. p. 267-85.

[31] LeCun Y, Bottou L, Bengio Y, Haffner P. Gradient-based learning applied to document recognition. Proceedings of the IEEE. 1998;86:2278-324.

[32] Refractive index database https://refractiveindex.info/